LAWRENCE
LIVERMORE
NATIONAL
LABORATORY

# Raman Spectroscopy and Microscopy of Individual Cells andCellular Components

J. Chan, S. Fore, S. Wachsmann-Hogiu, T. Huser

August 17, 2008

Lasers and Photonics Review

## Disclaimer

This document was prepared as an account of work sponsored by an agency of the United States government. Neither the United States government nor Lawrence Livermore National Security, LLC, nor any of their employees makes any warranty, expressed or implied, or assumes any legal liability or responsibility for the accuracy, completeness, or usefulness of any information, apparatus, product, or process disclosed, or represents that its use would not infringe privately owned rights. Reference herein to any specific commercial product, process, or service by trade name, trademark, manufacturer, or otherwise does not necessarily constitute or imply its endorsement, recommendation, or favoring by the United States government or Lawrence Livermore National Security, LLC. The views and opinions of authors expressed herein do not necessarily state or reflect those of the United States government or Lawrence Livermore National Security, LLC, and shall not be used for advertising or product endorsement purposes.

LLNL-JRNL-406312

# Title: Raman spectroscopy and microscopy of individual cells and cellular components

## Short title: Single Cell Raman Spectroscopy

**James Chan[1,2], Samantha Fore[1], Sebastian Wachsmann-Hogiu[1], and Thomas Huser[1,3]**

[1]NSF Center for Biophotonics Science and Technology, University of California, Davis, Sacramento, CA 95817, USA
[2]Physical Sciences Directorate, Lawrence Livermore National Laboratory, Livermore, CA 94550, USA
[3]Department of Internal Medicine, University of California, Davis, Sacramento, CA 95817, USA

## Abstract

Raman spectroscopy provides the unique opportunity to non-destructively analyze chemical concentrations on the submicron length scale in individual cells without the need for optical labels. This enables the rapid assessment of cellular biochemistry inside living cells, and it allows for their continuous analysis to determine cellular response to external events. Here, we review recent developments in the analysis of single cells, subcellular compartments, and chemical imaging based on Raman spectroscopic techniques. Spontaneous Raman spectroscopy provides for the full spectral assessment of cellular biochemistry, while coherent Raman techniques, such as coherent anti-Stokes Raman scattering is primarily used as an imaging tool comparable to confocal fluorescence microscopy. These techniques are complemented by surface-enhanced Raman spectroscopy, which provides higher sensitivity and local specificity, and also extends the techniques to chemical indicators, i.e. pH sensing. We review the strengths and weaknesses of each technique, demonstrate some of their applications and discuss their potential for future research in cell biology and biomedicine.

**Key words:** Raman spectroscopy, laser tweezers, coherent anti-Stokes Raman scattering, CARS microscopy, surface-enhanced Raman spectroscopy, SERS, nano-particles, time-correlated single photon counting, single cell microscopy

**PACS:** 33.20.Fb , 42.62.Be, 42.62.Fi, 42.65.Dr, 82.80.Gk, 87.17.-d, 87.18.Vf, 87.64.-t, 87.64.kp, 87.64.M-, 87.64.mk, 87.64.mn, 87.80.Cc, 87.85.fk, 87.85.Pq, 87.85.Rs

## Introduction

Our ever-increasing quest for a better understanding of the inner workings of cells and their communications amongst each other requires new tools and methods that enable us to follow cellular pathways and their changes in response to external events in living cells with minimal disturbance. Optical microscopy techniques are particularly useful in this regard, because they are widely available, relatively inexpensive, and readily adaptable to the environmental conditions necessary for live cell analysis. A wide range of fluorescent probes for molecular imaging have been developed over the last several decades, e.g. organic fluorescent dyes that can be conjugated to antibodies, fluorescent proteins that can be genetically encoded and fused to other proteins, or live cells fluorophores that can diffuse across the plasma membrane of cells and highlight specific organelles. These exogenous probes do, however, require specific knowledge about the cellular systems that they are used with, they have the potential to alter cellular function, their concentration changes with cell division, and ultimately, they all have a limited lifetime on the second to minute time scale, after which they undergo irreversible photobleaching and can no longer be probed. Other single cell analysis and imaging techniques, such as electron microscopy or secondary ion mass spectrometry (SIMS) can complement optical methods by providing higher spatial resolution or chemical information, but they either only work for frozen or fixed cells, or they destroy the cells during the analysis.

Thus, non-destructive optical methods that can continuously analyze living cells during their lifecycle, probe their interactions with other cells, and provide details about cellular chemistry are highly desired. Among these, Raman spectroscopy and imaging is rapidly gaining popularity, because it enables the non-destructive, label-free biochemical analysis of individual living cells, which complements other molecular, cellular, and physiological analysis techniques very well.

Raman spectroscopy is a powerful spectroscopic technique that allows for the identification of molecules based on the inelastic scattering of light by vibrational modes of chemical bonds within the molecule. The intensity of specific Raman spectral modes is given by the changes in molecular polarizability during vibrational transitions and is, therefore, complementary to infrared spectroscopy. There are several advantages of Raman spectroscopy: it requires no special dyes or specific excitation wavelengths, is mostly non-destructive and non-contaminating (depending on laser wavelength and power), and it can be combined with imaging modalities such as confocal and fluorescence microscopy, or with micromanipulation techniques like optical tweezers. Various techniques based on Raman scattering have been developed, including spontaneous Stokes and anti-Stokes Raman spectroscopy, Resonance Raman and time-resolved Resonance Raman Spectroscopy, Surfaced Enhanced Raman Spectroscopy (SERS), Coherent Anti-Stokes Raman Spectroscopy (CARS), Coherent Stokes Raman Spectroscopy (CSRS), Stimulated Raman Scattering (SRS), etc. (see Fig. 1).

The Raman effect has been experimentally discovered in 1928 by C. V. Raman and K. S. Krishnan [1]. In spontaneous Raman scattering, a small portion of the incident photons are scattered by interactions with chemical bonds resulting in a shift of the scattered photons toward lower frequencies, i.e., lower energy (Stokes-shifted Raman scattering). The energy difference corresponds to the vibrational energy of the specific molecular bond interrogated. A full Raman spectrum obtained from cells or tissues is an intrinsic molecular fingerprint of the sample, revealing detailed information about its macromolecular composition (DNA, RNA, protein, and lipid content), structure, and molecular interactions [2].

Anti-Stokes Raman spectroscopy relies on existing thermal energy within molecular vibrations to measure photons scattered at energies higher than the incident photons. While anti-Stokes Raman scattering is much weaker than Stokes Raman scattering and decreases exponentially with increasing vibrational energy (see Fig. 2a), there is significant information that can be obtained from these measurements. For example, the ratio between Stokes and anti-Stokes peak intensities can yield local molecular temperatures.

If the excitation light frequency approaches (pre-resonance condition) or equals (resonance condition) the frequency of an electronic transition of the molecule, the dependence of the molecular polarizability on the incident light frequency has to be considered, resulting in Raman intensities that are 3-4 orders of magnitude higher than in spontaneous Raman. Due to this Resonance Raman effect, Franck-Condon active vibrational modes that are coupled to the electronic transition are preferentially enhanced, revealing a somewhat less complex spectrum. The drawback of this technique is the high fluorescence background associated with radiative decay from the excited electronic state. Possible ways to avoid the fluorescence are setting the excitation laser in pre-resonance (on the blue side of the absorption spectrum) or using time-gated approaches that are based on the fact that fluorescence emission is orders of magnitude slower than Raman scattering [3, 4]. Currently, there are very few reports on Resonance Raman spectroscopy on live cells [5-8], since the excitation wavelength required for this experiment produces significant photodamage to the cells.

All the techniques mentioned earlier suffer from one major limitation that has somewhat hampered the wide application of Raman spectroscopy to cell biology. The intensity of the measured Raman signal is very weak due to the low cross-section for inelastic light scatttering, resulting in limited sensitivity of detection. In order to obtain Raman signals with excellent signal-to-noise ratio, millimolar molecular concentrations are typically required. Consequently, it can take up to several hours to acquire a typical spontaneous Raman image at the cellular length scale and other methods that allow for faster imaging, especially of living cells, are desirable. In the classical picture, the spontaneous Raman scattering is seen as a modulation of the oscillating dipole moment $p=\alpha E$ ($\alpha$ is the molecular polarizability and $E$ is the monochromatic radiation field) by a molecular vibration $\omega$, exhibiting Stokes and anti-Stokes frequencies (Fig. 1). Since this modulation is caused by the random-phased vibration of molecules, the emission is not coherent.

Coherent Raman scattering, on the other hand, stems from the forced molecular vibration generated by two different laser radiations $E_1$ and $E_2$ with frequencies $\omega_1$ and $\omega_2$, respectively. The vibrational motion is then generated in every molecule with a phase defined by the phase matching condition. Consequently, Raman scattering due to this vibration forms a coherent radiation field, which propagates along the axis of oscillating molecules. In this way, besides the incident frequencies $\omega_1$ and $\omega_2$, other frequencies $\omega_3=2\omega_1-\omega_2$ (for CARS) and $\omega_4=2\omega_2-\omega_1$ (for CSRS) are generated. A scheme showing the CARS enhancement over spontaneous Raman scattering is depicted in Fig. 2b. In a typical CARS or CSRS experiment, the pump source is a narrowband laser and the

Stokes beam can be narrowband or broadband, driving a single or multiple Raman vibrations, respectively. CARS has been initially developed to overcome the stronger fluorescence signal occurring on the Stokes side of the spectrum. The first report of imaging CARS dates back to 1982, when Duncan et al. [9] proved the feasibility of such a microscope using picosecond pulsed lasers. This technique did, however, not gain significant traction until 1999, when the seminal paper by Zumbusch et al. [10] demonstrated the use of CARS microscopy for living cells with moderate average power for excitation under tight focusing conditions. Since then, CARS has become the topic of intense research and development, with increasingly diverse biological and biomedical applications. The most common CARS arrangements currently use a pump laser that synchronously pumps one or two additional lasers, generating the Stokes wavelengths necessary to drive up to three different Raman vibrations. By selectively choosing Raman vibrations specific for molecules of interest, quantitative Raman analysis can be performed by measuring the ratio between the Raman intensities.

Another mechanism that enhances the cross section for Raman scattering is observed in the presence of rough metallic structures or nanoparticles. Surface-enhanced Raman scattering (SERS), a phenomenon discovered in 1977 [11], takes advantage of large effective Raman cross sections approaching or comparable with effective fluorescence cross sections for molecules attached to or near nanometer-sized metallic structures [12-14]. Large enhancement factors, on the order of $10^{15}$ have been reported, making it possible to perform Raman measurements even on the scale of single molecules. While the chemical enhancement factor (a dynamic charge transfer between the molecule and metal) accounts for two to three orders of magnitude in enhancement, the largest contribution to the huge SERS cross sections seems to come from the electromagnetic or field enhancement factor (enhanced local electric field at the place of the molecule nearby the metal surface due to collective excitation of conduction electrons within the small metallic structure). The utility of the SERS effect in measuring biological effects on the nanoscale is obvious, and much effort has been directed not only towards the understanding and control of the SERS process, but also towards the functionalization of metallic nanoparticles that turns them into cellular nanoprobes.

A typical, generalized Raman imaging setup is shown in Fig. 3. To obtain an image, either the monochromatic excitation light or the object is scanned. The Raman signal is collected and passed through a spectral tuning element before reaching the detector. The tuning element can be either a spatial scanning device such as a single or multiple slit spectrometer with a dispersive element (prism or grating), or a wavelength scanning device such as acousto-optical tunable filter (AOTF) or liquid crystal tunable filter (LCTF). While spatial scanning techniques can achieve high spectral resolution and are the method of choice for most Raman imaging experiments, wavelength scanning techniques have limited spectral resolution, but offer higher speed, which is essential for most biomedical applications.

## 1. Spontaneous Raman spectroscopy of single cells

Single cell Raman spectroscopy was first achieved almost 20 years ago through seminal work by Puppels et al. [15] which combined spontaneous Raman spectroscopy with confocal microscopy to enable the noninvasive and nondestructive biochemical analysis of femtoliter volumes within a biological sample. Since then, spontaneous micro-Raman spectroscopy has taken significant strides toward becoming an accepted technique in the biological sciences for investigating the biochemistry of single cells, micro-organisms, and subcellular components. Applications in a wide variety of fields, such as microbiology [16-18], cancer research [19-21], and cardiovascular research [22-24] have been demonstrated. The ability to perform label-free analysis and imaging of the intrinsic biochemical composition of a living cell makes this method very attractive since it significantly expands and complements conventional brightfield and fluorescence microscopy. Also, unlike fluorescence signals that may photobleach over time, Raman signals are persistent and therefore enable long term interrogation of the same cell for monitoring cell dynamics. As a non-invasive and non-destructive technique that can be easily implemented into existing microscopes and instruments, Raman spectroscopy can be a complementary tool to other techniques for the multi-modal analysis of the same sample.

Amongst other, more sensitive forms of Raman spectroscopy (e.g. CARS and SERS - two techniques that are also discussed in this article), spontaneous Raman spectroscopy remains an attractive biophotonic analysis method for minute sample volumes, because it is the most robust, user-friendly, and established method, and micro-Raman systems are readily commercial available. While SERS requires the incorporation of nanoparticles for intracellular chemical sensing, spontaneous Raman spectroscopy is a completely non-invasive, label-free method that does not require the addition of any analytes or exogenous probes. CARS holds promise to eventually supplant spontaneous Raman spectroscopy for rapid imaging and spectroscopic analysis due to its stronger signals. Currently, however, it still requires simple solutions to technical hurdles such as background contributions from nonresonant signals that have restricted its application mostly to imaging of strong vibrational modes (i.e. abundant lipid vibrations), while imaging DNA and protein modes remains a challenge. Fundamentally, CARS imaging does not offer any new biochemical signatures that could not otherwise be obtained by spontaneous Raman spectroscopy. Also, CARS microscopy still relies heavily on Raman spectroscopy; prior to CARS imaging characterization of the full Raman fingerprint of the sample by spontaneous Raman spectroscopy is often needed. CARS instrumentation is currently still too expensive, large, and complex for practical use in biological laboratories. As such, it is a technique that remains in its early stages and requires further development.

### *1.1 Raman point spectroscopy and imaging of single cells*

The basic principle of micro-Raman spectroscopy for single cell point spectroscopy or imaging applications is the efficient confocal detection of Raman signals while minimizing background contributions from areas outside the laser focus, as shown in the schematic illustration of a confocal Raman microscope (see Fig. 4a). Epi-illumination with a tightly focused laser beam directed at a desired region within the sample maximizes local Raman excitation while delivering minimal light to other regions. A pinhole conjugate to the focal point allows the Raman scattered light to pass through to the detector while rejecting out of focus background signals in both the axial and lateral directions. In our system, we use an 80 mW, 785 nm diode pumped solid-state laser (Crystalaser, Reno, NV) combined with an optical isolator as the Raman excitation source. Near-infrared excitation light is typically chosen for micro-Raman spectroscopy because at these wavelengths absorption by most biological molecules is minimal, which reduces the potential for photodamage to cells and tissues or fluorescence excitation of endogenous fluorophores. An inverted microscope (Olympus IX-71) equipped with a 60x 1.2 NA water immersion objective and a dichroic mirror (810DRLP, Chroma Filters, Brattleboro, VT) delivers the light to a sample typically mounted on a glass or quartz coverslip. The sample is held in an x-y translation stage, which can be actuated for Raman imaging or manually controlled for precise positioning of the laser probe beam. Raman signals are collected by the same microscope objective, passed through a 75 µm diameter pinhole, filtered with a steep edge long pass filter (785nm RazorEdge, Semrock, Inc, Rochester NY), and dispersed onto a back-illuminated thermoelectrically cooled deep-depletion CCD camera with 1340x100 pixels (PIXIS:100BR, Roper Scientific, Trenton, NJ) by a 600 groove/mm reflection grating blazed at 1 µm wavelength inside a 0.3 m spectrometer.

For point spectroscopy, the position of the sample is moved with respect to the laser focus to interrogate different regions of the sample with diffraction-limited spatial resolution. An example is shown in Fig. 4b, which shows a brightfield image of a single living human immune cell (THP-1 monocyte, ATCC, Manassas, VA), which was allowed to adhere to a quartz glass substrate. Also shown is a fluorescence image of the same monocyte after staining with Hoechst 33342, a fluorescent live cell stain that specifically stains DNA. Raman spectra acquired from the nuclear and cytoplasmic regions of this monocyte clearly show differences in their local biochemical composition. The spectrum of the nucleus reflects strong signals from DNA (e.g. a cytosine ring-breathing mode at 785 $\text{cm}^{-1}$) as well as several strong Raman modes that are indicative of the presence of the Hoechst dye in the nucleus (e.g. at 1558 $\text{cm}^{-1}$ and 1607 $\text{cm}^{-1}$), while the spectrum of the cytoplasm shows significantly lower signal intensities at these peak positions. Raman imaging (or mapping) is in essence based on the same concept as point spectroscopy, but requires more precise and reproducible two-dimensional positioning of the sample, which is typically achieved by using a nano-positioning stage. With the help of such an actuated stage all regions within the cell can be precisely probed and a chemical map (or: Raman image) of the sample can then be reconstructed by post-analysis of specific peak intensities. Typically, a certain area within the sample is first chosen for Raman mapping and divided into small squares, which can be considered Raman pixels - limited only by the dimensions of the probe beam. Raman point spectroscopy is performed on each of these defined Raman pixels, and, following background subtraction and normalization of the data, each pixel is assigned an intensity value based on the strength of a particular Raman marker of interest. By repeating this procedure for different Raman bands, Raman images showing the spatial distribution of biomolecules, such as DNA, proteins, and lipids can be constructed. Raman mapping based on intrinsic vibrational markers provides a unique approach to label-free chemical imaging. Several studies have applied Raman mapping to tissues and even individual cells. For example, deJong et al. [19] used Raman imaging to demarcate tumor and nontumor regions in bladder tissue. Several groups have used this approach to visualize the protein and DNA distribution in normal and apoptotic cells [25, 26], chemical distributions associated with the bioactivity of single cells [27-29], or for identifying differences in the spatial distributions between benign and malignant prostatic cells [20].

A significant limitation of this technique, however, is the fairly long time that it can take to obtain a full Raman image (typically up to several hours), because a full Raman spectrum has to be obtained for each pixel of the image. This typically requires cells to be fixed, which obviously limits its application for live cell imaging. This major drawback is the main driving force for the development of CARS microscopy, which will be discussed in the next section. By employing alternative approaches, e.g. by modifying the sample illumination to a line-scan approach [30, 31] or employing novel electron-multiplying CCD cameras, the imaging time for spontaneous Raman imaging can also be significantly reduced, making it still an attractive method for label-free cell imaging. Fig. 5 illustrates the main difference between the point and line scanning approach. Point scanning requires sample scanning in both lateral directions. On the detection side, the focal point region is imaged onto the spectrometer slit as a single point, and the Raman signal is subsequently dispersed onto a detector as a single line. Laser line scanning, on the other hand, reshapes the beam as it enters the microscope objective using cylindrical lenses so that the sample is illuminated with a line focus, which can be viewed as the equivalent of multiple foci aligned along one axis of the sample. By projecting the line through the slit onto a CCD camera, spectral information from the entire illuminated line can be recorded. Therefore, scanning in only one axis is required, which significantly reduces the acquisition time and permits live cell imaging with spontaneous Raman spectroscopy within a few minutes.

### *1.2. Laser trapping and Raman spectroscopy*

For individual biological particles with a size between ~100 nm to 1 μm diameter, it becomes increasingly more difficult to perform micro-Raman spectroscopy since it is difficult to address the samples because of their small size. Typically, such small particles can only be immobilized on a glass surface by drying the samples on the substrate, which may compromise their biological activity. Also, these particles are difficult to visualize and have to be located first by scanning the laser across the substrate surface to generate backscatter or autofluorescence images. Then, the laser focus has to be repositioned onto the particle for Raman interrogation. The same difficulties apply to non-adherent cells such as blood cells that are naturally suspended in a liquid environment and which are difficult to probe because Brownian motion leads to diffusion of cells in and out of the laser focus during the spectral acquisition time. Chemical immobilization of the cell could circumvent this problem, but may lead to cell activation and produce undesired cellular responses.

The combination of optical tweezers (i.e. optical trapping) and Raman spectroscopy has proven to be an innovative approach for analyzing these challenging biological samples [32-36]. Optical tweezers are created by focusing a laser beam to a tight spot to generate radiation forces that physically immobilize a single particle within the laser focus [37, 38]. Fig. 6a illustrates the principle behind optical tweezers based on ray optics. A light ray refracted by the surfaces of a transparent object undergoes a change in photon momentum and a corresponding force is imparted onto the particle in the opposite direction. Because of the Gaussian shape of the intensity profile of the laser beam, a ray refracted near the center of the beam induces a much stronger reaction force on the particle than rays near the circumference. The net result is a force, $F_{lat}$, which drives the particle towards the center of the beam, resulting in an equilibrium lateral position at the center of the focus, as illustrated in Fig. 6b. A similar argument can be made for axial forces, $F_{ax}$, resulting from the inhomogeneous on-axis intensity distribution in a tightly focused laser beam that leads to the particle being pulled towards the center of the laser focus. Additional forces present in this geometry include a scattering force, $F_s$, in the direction of the light propagation and gravitational forces $F_g$. The need for a tight focus to stably trap a particle within a single beam is mainly governed by the high axial forces, $F_{ax}$, that are required in order to overcome the scattering forces working against the axial force. The need for tight focusing by both optical trapping and micro-Raman spectroscopy makes the combination of both methods ideal and straightforward.

Multiple optical configurations have been demonstrated for laser trapping Raman spectroscopy (LTRS). The simplest configuration to implement, and the one that has been used the most extensively by our group, is a single beam approach as illustrated in Fig. 7a. Here, a single laser beam is used to both optically trap cells and to obtain their Raman spectrum. Another, closely related approach with the same optical configuration uses two collinear laser beams with different wavelengths [36]. Such an arrangement can be desirable if high laser powers are needed to trap microscale objects for which absorption at red or near-infrared wavelengths might induce photodamage. Here, a high power laser at 1064 nm wavelength can be used for optical trapping, while a low power, shorter wavelength (e.g. 633 nm) laser is then used for Raman scattering. The shorter wavelength generates stronger Raman signals, since the Raman scattering intensity is proportional to the frequency to the fourth power. Decoupling of the laser trap and Raman probe laser also allows for the Raman excitation beam to be reshaped and e.g. to be scanned across the entire optically trapped sample if the sample dimensions exceed the size of the focused laser spot. A second configuration utilizing two tightly focused counter-propagating laser beams (Fig. 7b) can be desirable if a single tightly focused beam does not provide sufficient axial radiation forces to trap an object. This counter-propagating design also enables optical trapping with lower numerical aperture microscope objectives. A third configuration (Fig. 7c), demonstrated by Jess et. al [39], involves using dual optical fibers for trapping large (30 μm) diameter cells and an additional objective positioned perpendicular to the fiber axis for delivering the interrogating laser beam.

Fig. 8 shows the range of different particle types and sizes that can be analyzed by LTRS. All spectra shown in this Figure were obtained using the single beam laser trap configuration. For small particles (i.e. less than ~ 0.5 μm diameter), it is difficult to visually determine when a particle is trapped by conventional transmitted light microscopy. In this case, an optically trapped particle is visualized by observing the backreflected laser light from the trapped particle. To obtain confirmation that truly just a single particle is trapped is often difficult, but can e.g. be determined by observing intensity fluctuations of the backscattered light which are caused by diffusion of the particle within the dimensions of the optical trap. We have trapped individual cellular organelles such as mitochondria isolated from rat kidney cells or single triglyceride-rich lipoprotein (TGRL) particles isolated from blood. For large particles with a diameter > 2 μm, single objects can clearly be observed by white light imaging. Raman analyses of bacterial spores (Bacillus cereus) and E. coli cells have been performed in our laboratory. For even larger objects such as cells with a diameter of ~10-20 μm, optical trapping is still feasible, but because of the small dimensions of the laser spot (~ 1 $\mu m^3$), only a small fraction of the cell is optically trapped. In many cases, a particular organelle of high index of refraction (e.g. the cell's nucleus) will be consistently trapped. Consequently, the acquired Raman spectrum reflects only a fraction of the total cell's biochemical composition. Raman spectra of smaller cells, such as bacterial cells, however, more accurately reflect the overall biochemical composition of the cell. This important point needs to be considered when applying LTRS to the analysis of large cells. An alternative optical design using two laser beams, one tightly focused for optical trapping and a second beam reshaped to illuminate a larger fraction of the cell volume or scanned over the entire cell, may be more appropriate in these situations.

One of the first biomedical applications of LTRS used by our group [2] was the analysis of normal cells and cancer cells at the single cell level. The primary goal of these studies was to identify unique, label-free Raman markers that could accurately discriminate between normal and cancer cells. A label-free, non-destructive approach provides the added benefit of allowing us to track and monitor living cells over long periods of time, or to isolate populations of cells that are not contaminated by optical labels, i.e. fluorophores. Figure 9a shows the mean Raman spectra of three different groups of T lymphocytes – normal T cells from a healthy volunteer, transformed T lymphocytes from a T cell cancer cell line (Jurkat T, ATCC, Manassas, VA), and cancer T cells from a leukemia patient. We found that the Raman spectra of cancer cell populations exhibit consistently lower DNA to protein peak intensity ratios when compared to spectra of normal cells. This difference is particularly apparent in the difference spectra shown in Fig. 9b and possibly indicates differences in the local nuclear DNA-protein concentration of the cells, the packaging of the chromatin, and the molecular configuration of chromatin as a result of the different levels of transcription in these cells. To better compare the complex spectra obtained by Raman spectroscopy, we employ Principal Component Analysis (PCA), a common multivariate statistical method that is often used to reduce dimensionality and to identify combinations of the most important spectral markers that maximizes the data variance and optimizes group separation. PCA yields scatter plots that can be used to visualize the separation of the cell groups (Fig. 9c). When applied to our data of leukemic cells, we observe that the cancer and transformed cells can be routinely separated from normal cells with >90% sensitivity. Similar results were observed for B lymphocytes.

Taking advantage of the ability to analyze submicron-sized particles, another application of LTRS in our group was to characterize triglyceride-rich lipoproteins (TGRLs) [40], which are small (10 nm - 1 μm diameter) lipid particles in blood that are responsible for the transport of triglycerides and cholesterol throughout the body. By analyzing TGRL particles derived from human volunteers after an 8 hour fasting period and 3 and 8 hour post-consumption of well-defined diets by Raman spectroscopy, we were able to determine that differences in the Raman fingerprints of pre- and postprandial particles, in particular in the 1000-1200 $cm^{-1}$ region of the fingerprint spectrum, indicate that lipid structures within postprandial particles exhibit an increased level of saturation and a higher degree of ordered stacking of the hydrocarbon chains. This chemical change is believed to be related to the hydrolysis of triglycerides stored in these lipid particles following the exposure to lipoprotein lipase (LpL), and enzyme in the endothelial cell membrane. We confirmed this result by performing in-vitro experiments exposing isolated particles to LpL and observed a similar spectral response.

Monitoring dynamic processes of a single cell over long periods of time is difficult with standard fluorescence-based techniques due to photobleaching of the fluorophores, which results in significant signal degradation over time. Because Raman spectroscopy is a scattering process it typically provides robust and reproducible signals that can be used to continuously monitor cellular processes. LTRS is particularly useful in this case because a single cell can be consistently monitored in response to external events such as the elevation of the temperature or the introduction of chemicals into the surrounding solution. Our group has used time-resolved LTRS to monitor the overexpression of proteins in single cells over a three hour time frame [41]. Single transfected E. coli bacterial cells were induced to overexpress myelin oligodendrocyte glycoprotein (MOG) upon exposure to isopropyl thiogalactoside (IPTG). Over the course of three hours, Raman spectra continuously taken from E. coli cells revealed gradual increases in several protein marker modes (e.g. 1257, 1340, 1453, 1660 $cm^{-1}$). From the change in the peak intensities, it was estimated that a 470% increase in protein concentration at the first and second hour time points occurred, which then leveled off to a 230% increase between the second and third hour. It is not possible to obtain this type of information at the single cell level with conventional bioanalytical approaches such as sodium dodecyl sulphate polyacrylamide gel electrophoresis (SDS PAGE), which only reveals averaged information from many thousands of cells at one specific time point. A similar study [42] was recently performed by Xie et al. to detect recombinant somatolactin protein in single E. coli bacteria and Pichia pastoris yeast cells. A variety of other biological systems have been studied using the LTRS approach. The use of LTRS to monitor cell growth phases [43], spore germination [44], hyperosmotic stress response in yeast cells [45], activation-dependent phases of T cells [46], and the response of red blood cells to alcohol exposure [47], have all been reported over the past five years. These studies have built a strong foundation for LTRS as a tool to monitor single cell dynamics and better understand the variations in the response of individual cells within a heterogeneous cell population.

## 2. Coherent Raman microscopy of individual cells

The chemical analysis of cells by spontaneous Raman scattering, as described above, is typically used as a purely spectroscopic technique, yielding quantitative information about the molecular composition and the structure of single cells. Although, as briefly mentioned above, spontaneous Raman scattering can also be applied to image biological specimens such as cells and tissue sections, due to the rather weak signals, acquisition times can vary from several minutes up to several hours [48-51]. Thus, the observation of fast dynamics within cells such as vesicular trafficking or diffusion is clearly not possible, and sample viability can also be compromised after such long data acquisition times. The use of coherent anti-Stokes Raman scattering (CARS) for the chemically selective imaging of molecular constituents within a biological specimen circumvents these problems due to a significant increase in signal, which decreases the time necessary to acquire an image. This gain in signal has recently even enabled CARS imaging at video rate speeds in-vivo and ex-vivo [52-66].

As briefly outlined in the introduction, CARS is a nonlinear optical (NLO) phenomenon where the CARS signal arises from the third order induced polarization, $P^{(3)} = \chi^{(3)}E_pE_sE_p$, in the sample. As such, it occurs in any material exhibiting a nonzero third-order susceptibility $\chi^{(3)}$. When the frequency difference between pump and Stokes fields is tuned to, or is in resonance with, the frequency of a Raman active vibration, $\omega_{vib}$, of the material, the anti-Stokes signal is significantly enhanced. While this is a great advantage of the nonlinear optical properties of CARS, there is also always a non-resonant contribution present due to the electronic properties of the material, which presents a significant source of background signal in any CARS application. When on resonance with $\omega_{vib}$, all the molecular bonds represented by this vibrational frequency in a given excitation volume oscillate in phase, i.e. coherently. Furthermore, since CARS is a four-wave mixing process, it is crucial that the phase-matching condition is met between all of the associated fields. Indeed, in the first demonstration of CARS microscopy, a non-collinear beam geometry was employed [9]. This, however, severely limited the use of CARS in microscopic applications, as alignment was tedious and difficult to maintain. However, a renaissance in CARS was experienced when the relaxation of the phase matching condition was introduced under the conditions of tightly focused laser beams [10]. This was accomplished through the use of collinear beams and high numerical aperture objectives, thereby also improving the spatial resolution for imaging and decreasing the average power necessary to achieve sufficient CARS signals.

Because CARS is a nonlinear optical effect, the use of pulsed laser sources with high peak power is necessary. Unlike two-photon fluorescence excitation, however, which typically requires the use of femtosecond pulsed laser sources to achieve the necessary power density for two-photon absorption, CARS only requires the use of picosecond laser pulses. In fact, it was found that the use of picosecond pulses was advantageous due to the narrow spectral width of the Raman transitions [67, 68]. The broad spectral distribution of femtosecond laser pulses leads to an increase of the non-resonant signal, and conversely, the use of the spectrally narrower pulses decreases it. Even with the implementation of the collinear beam excitation, CARS microscopy is somewhat challenging to realize in practice. Both, the Stokes and pump-probe beams must be spatially and temporally overlapped at the sample. Furthermore, to cover the broad distribution of Raman vibrational transitions that are pertinent to biological systems, a laser source with a large range of wavelength tuning is required. This was first accomplished through the use of tunable dye lasers [9], and then with Ti-Sapphire lasers [10], both of which have to be synchronized to maintain the temporal relationship between pulses at different wavelengths. In the past few years, with the development of new, and more stable optical parametric oscillators (OPO), the CARS community has seen a transition to the use of OPO sources pumped e.g. by a 1064 nm laser that can also serve as the Stokes beam [52, 69-71]. Thus, a simple optical delay path inserted in the beam path of the Stokes beam is all that is necessary to account for the extra distance the pulses propagate inside the OPO cavity to achieve temporal overlap at the sample. A typical CARS setup is shown in Figure 10a, and will be explained in more detail further below. CARS excitation is most commonly achieved with sources in the infrared wavelength range. This has several advantages for biological specimens. Since the light sources are at longer wavelengths, there is less absorption in the material and thus, less potential for sample damage [72]. Furthermore, the longer wavelengths can penetrate deeper into thick tissue samples [73]. The background due to one-photon excited fluorescence is also substantially reduced. However, the use of longer wavelengths is not without its disadvantages. Specifically, it decreases the ultimate optical resolution that can be achieved. Due to the nonlinear optical nature of the CARS process, a slight improvement in the resolution is still achieved, especially in the axial directions, and thus, CARS also has inherent optical sectioning capability. Finally, CARS can be combined with several other nonlinear optical imaging modalities, including two-photon excited fluorescence (TPEF) and second harmonic generation (SHG), to provide additional unique information [74, 75].

A basic diagram of the optical layout of our CARS imaging system is shown in Figure 10a. In this system the 1064 nm line of a Nd:$YVO_4$ laser (Picotrain, High Q Laser, Austria) with 10 W average power and 7 ps pulse width at 76 Mhz repetition rate is used to simultaneously pump an optical parametric oscillator (OPO – Levante, APE, Berlin, Germany) for the generation of the pump-probe pulses and to serve as the Stokes beam. Most of the 1064 nm power (9 W) is used to synchronously pump the OPO, and only the remaining 1 W is used as Stokes source. This generates approximately 1.5 W of OPO average power with 6 ps pulse width, and wavelengths tunable from 770 nm to 960 nm. The two beams are combined using a dichroic mirror (Chroma Technology Corp., Rockingham, VT), and then sent through an electro-optical pulse picker (M350-160, Conoptics, Danbury, CT) to reduce the pulse repetition rate to 7.6 MHz in order to minimize photo-induced thermal damage while maintaining high pulse energy. The combined laser beams are then sent into an inverted optical microscope (IX71, Olympus America, Center Valley, PA), reflected by a 750 nm short pass dichroic mirror (Chroma Technology) and focused onto the sample by a 60x, 1.2 NA water immersion objective (Olympus) to form a diffraction-limited spot at the sample. The epi-CARS signal is collected by the same microscope objective, spectrally separated from the excitation sources by the dichroic mirror and a set of bandpass filters, i.e. a multiphoton short-pass filter (FF-01-750, Semrock, Rochester, NY) and a 40 nm wide bandpass filter (#42-7377, Ealing Catalog, Inc., Rocklin, CA) around 660 nm, before being focused onto a single photon counting avalanche photodiode (SPAD, SPCM-AQR 14, Perkin-Elmer, Waltham, MA). A portion of the CARS signal is also sent to a spectrometer (Acton SpectraPro 2300i, PI Acton, Trenton, NJ) equipped with a back-illuminated deep-depletion charge-coupled device (CCD) camera (PIXIS 100BR, PI Acton, Trenton, NJ). For all images shown in this review, the OPO wavelength was tuned to match the aliphatic C-H stretch mode at 2845 $cm^{-1}$ (see Fig. 10b). The sample is scanned using objective scanning, where the objective is held in a piezo-actuated closed-loop xy translation and objective focusing stage (Model P-733.2CL and P-721.CLQ, Physik

Instrumente, Irvine, CA) which provides 80 μm x 80 μm x 80 μm translation range to scan the sample. Alternatively, sample scanning, where the sample is held on and moved by the piezo stage is also employed. Examples of images collected using the 2845 $cm^{-1}$ line are shown in Fig. 10c and 10d.

### *2.1. CARS microscopy applied to biological samples*

As discussed above, in many aspects, CARS is ideally suited for the study of biological specimens and for many biomedical applications. The growing list of publications dealing with these applications is proof that CARS holds promise for the future of non-invasive imaging from cellular systems to large animals [52, 54, 56-60, 62-64, 66]. However, the major disadvantage of CARS is the existence of the nonresonant background. Indeed, there have been many developments in the field that aim to suppress or reduce this contribution, such as polarization sensitive detection [76], time-resolved detection [77, 78], and frequency modulation CARS [79], to name a few. The goal of any CARS application in the biological field, however, should be simplicity of implementation, so that this technique can be made accessible to a wider range of researchers. This is not always the case for the above-mentioned solutions. Fortunately, some other simple solutions that can aid in reducing the non-resonant contribution exist. Most of the CARS signal is scattered in the forward direction, and this is especially true for the non-resonant background. However, for features with a size on the order of the wavelength or less, there is a significant portion of the CARS signal that is scattered in the epi-direction [67], which is the same optical configuration used in most one-photon confocal fluorescence microscopes. For imaging of cellular components this geometry is ideal. Another simple method to increase the resonant to non-resonant signal ratio is to use the C-H stretch vibration for CARS imaging. As the resonant CARS signal is proportional to the number of bonds present in the excitation volume, and as biological samples are rich in C-H bonds, especially in lipids, the relative background contribution due to the non-resonant signal is substantially weaker in comparison. The use of this Raman transition for CARS imaging has been demonstrated in many applications [53], including CARS imaging of the myelin sheath in the central nervous system [66], the trafficking of lipid bodies in Y-1 cells [62], and imaging of lipid bodies in adipocytes derived from mesenchymal stem cells [80], to name a few. Despite the limitation of using only one Raman transition, there are many interesting applications that can be addressed. For example, various forms of lipids, in particular triglycerides, and the lipoprotein particles that transport them in the blood, are an important factor in the processes that lead to cardiovascular disease (CVD), especially atherosclerosis. Also, intimately linked to CVD is the growing epidemic of obesity worldwide. Both of these areas involve the intricate interplay between lipids and cells in our bodies. Having a method that can image these interactions with chemical specificity over long periods of time without the need for exogenous labels and *in vivo* is invaluable to both the scientists studying and the medical community diagnosing and treating these diseases. The imaging of atheroma in the iliac artery of a pig on a high fat diet has recently been demonstrated by Le et al. [75]. We have also seen the result of treatments with lipids and triglycerides on other cells involved in these diseases, which e.g. result in the formation of lipid droplets in monocytes and hepatocytes as shown in Figs. 10c and 10d.

In order to image other Raman modes, especially those associated with proteins and other molecules of biological interest, it is necessary to implement a method that improves the signal to non-resonant background ratio. As discussed previously, there are schemes available to accomplish the reduction of the non-resonant contribution, such as polarization-sensitive detection [76] and epi-CARS detection [67]. However, most of them come at the cost of complexity and typically also lead to a concurrent reduction in the resonant CARS signal. A promising approach to applying CARS imaging to vibrational bands other than the aliphatic C-H stretch modes, is to simultaneously image two different Raman modes using three synchronized laser pulses and perform ratiometric imaging to eliminate the contribution from the non-resonant signal. This has recently been demonstrated by Burkacky et al. [52] using the 2845 $cm^{-1}$ C-H aliphatic mode and a deuterated C-D mode at 2115 $cm^{-1}$. However, to our knowledge, this method has yet to be demonstrated with natural non-lipid Raman modes.

As mentioned earlier, CARS can be readily combined with other NLO imaging modalities, such as TPEF, SHG and third harmonic generation (THG), as each technique has its unique advantages, e.g. SHG is sensitive to non-centrosymmetric structures such as collagen networks and THG is sensitive to interfaces [74, 75]. TPEF can be applied to simultaneously visualize the fluorescence from fluorescent proteins or other fluorescently labeled molecules [62], as well as the auto-fluorescence from endogenous fluorophores or structures. However, the former is contrary to the argument for label-free detection, and the latter is often a significant source of background in the CARS detection channel. Depending on the type of tissue, this background fluorescence can exhibit significant spectral overlap with the CARS signal and often mask it. In particular, tissues that are in contact with blood, have other sources of broadband autofluorescence in a similar wavelength range, which stem from e.g. porphyrins and heme chromophores. To date, suppressing these autofluorescent signals in CARS imaging has been limited to the use of narrow bandpass filters centered around the CARS signal. This solution has several limitations, one of which is the suppression of the CARS signal itself, due to the reduced transmission of narrow bandpass filters. We have been exploring the use of time-resolved signal detection methods (not to be confused with the time-resolved CARS methods used to reduce the non-resonant background contribution), to combine CARS with TPEF in a manner in which the two signals can be collected simultaneously and separated post imaging using time gating.

Since Raman spectroscopy is based on inelastic light scattering rather than electronic excitations, it is a quasi-instantaneous process with decay times orders of magnitude faster than fluorescence excitation. This is sometimes used in spontaneous Raman spectroscopy of bulk samples, where fast optical gates can be employed to separate the Raman scattering from the typical nanosecond excited state lifetimes that are characteristic of fluorescence emission. By implementing a time-correlated single photon counting (TCSPC) detection scheme similar to what has been previously reported for fluorescence lifetime imaging (FLIM) [81-84], we are able to use the photon arrival time information to discriminate between the quasi-instantaneous CARS photons and the delayed two-photon excited autofluorescence photons. The details of TCSPC are illustrated in Figs. 11a and 11b. Photon counts from the photon-counting detector, such as an avalanche photodiode (APD) are used as the start signal and the electronic reference signal from the laser is used as the stop signal for a time-correlated single-photon counting system (TimeHarp200, PicoQuant GmbH, Berlin, Germany). Data collection, image scan synchronization, and data analysis is achieved by a commercial software package (SymPhoTime, PicoQuant GmbH, Berlin, Germany). The TCSPC board is operated in Time-Tagged Time Resolved (TTTR) mode, which records both, the microscopic arrival time of each photon (the time between start and stop pulses) with picosecond time resolution, as well as the macroscopic (absolute) arrival time with 100 ns precision [85-87]. The instrument response function (IRF) of our CARS system was measured to be ~330 ps at 650 nm wavelength [88]. Software time-gating allows us to separate photons that arrive within the IRF and correspond to photons emitting by the CARS process (blue shaded region in Figure 11c), from photons arriving in the "tail" of the decay in the TCSPC window which correspond to TPE fluorescence photons (red shaded region.) By laterally scanning the sample, the average "lifetime" or microscopic arrival time for each pixel of an image can be measured similar to the standard FLIM scheme. If a color scale is defined for the measured lifetime range, an image similar to that shown in Fig. 12a can be constructed [88]. Here, a cross-section of an artery from a healthy rat is shown. Areas that show up in blue color correspond to photon arrival times of 0.6 ns or less, and can thus be assigned to CARS photons. The green to red colored regions correspond to photon arrival times of > 1.2 ns, and can be assigned to two-photon excited tissue autofluorescence. As can be seen from this image, the photon arrival times of less than 0.6 ns (blue regions) indicate the presence of a number of small, discrete regions within the tissue near the arterial lumen that exhibit very strong lipid vibrations. We tentatively assign these areas to temporary small, lipid-rich deposits as rats do not typically suffer from cardiovascular disease and their associated saturated fatty acid deposits. Finally, by applying software time gates, i.e. the blue and red regions in Fig. 11c, the CARS and TPE autofluorescence photons can be separated to create images that contain in essence only CARS photons or only fluorescence photons as shown in Fig. 12b and 12c, respectively.

### *2.2. Separation of epi-CARS and forward CARS signals by TCSPC*

More recently, we have also demonstrated that TCSPC can be used to separate epi-directed (E-CARS) and forward-directed CARS (F-CARS) signals detected by a single photodetector [80]. Here, F-CARS signals are back-reflected by a mirror, adjusted in height to provide an appropriate time delay between the E-CARS photons and the forward-directed CARS photons. The optical layout of this scheme is shown in Fig. 13a, and differs from the previously described setup only by an additional condenser lens which is used to collect forward CARS photons and a mirror placed above the sample. The details of this set up have been described elsewhere [80]. The additional time delay between the two CARS signals manifests itself in the appearance of two "bumps" in the photon arrival time histogram, indicating the onset of the E-CARS (green line in Fig. 13b) and the F-CARS signals (red line). By assigning false colors to these two regions in the photon arrival time distribution, a single image indicating the E-CARS and F-CARS contributions can be constructed using the photons detected by a single detector, compared to other CARS schemes that require two separate detectors to collect both E- and F-CARS. This scheme can be advantageous in CARS applications that impose tight spatial constraints or where a significant portion of the F-CARS signal is intrinsically back-reflected, e.g. in tissue imaging. An example of the power of this technique is shown in Fig. 13c where we imaged an adipocyte derived from human mesenchymal stem cells (hMSC). After induction of their differentiation into adipocytes, MSCs begin to form characteristic lipid-filled droplets that spread throughout their entire cytoplasm. The lipid droplets provide a strong CARS signal due to the symmetrical stretch vibration of the aliphatic lipid $CH_2$ bond at 2845 $cm^{-1}$. These lipid droplets grow to a size larger than the wavelength used for CARS microscopy, and thus, most of the CARS signal is scattered in the forward direction. The E-CARS signal, however, becomes significant for small droplets or near the edge of large droplets as expected. The false color in the image shows F-CARS signals in red and E-CARS signals in green. Also shown in Figure 13d are E- and F-CARS line scans as indicated by the white line in Figure 13c. Thus, this technique demonstrates that the simultaneous detection of forward and backward-directed CARS microscopy signals through back-reflection by a mirror leads to maximized CARS signal collection.

## 3. Surface-enhanced Raman spectroscopy of cellular components

As we have seen in the previous two sections, confocal micro-Raman imaging and spectroscopy is a valuable, label-free technique for the nondestructive chemical analysis of single cells with a spatial resolution comparable to that of fluorescence microscopy. For Raman spectroscopy to become widely accepted by the cell biology community, however, certain limitations still need to be overcome. Most prominently amongst these is the fact that Raman spectroscopy requires typically at least millimolar concentrations to result in high quality spectra (i.e. a signal to noise ratio ~ 10:1). Even at such high concentrations, spontaneous Raman spectroscopy still requires signal acquisition times on the order of several seconds. Lastly, while Raman spectroscopy can probe and identify most chemicals in a cell it does not provide the phenotypic molecular specificity that can be achieved by fluorescently labeled antibodies. Raman spectroscopy is usually only sensitive to the most abundant molecular species, and it is also not typically sensitive to specific chemical states, i.e. ion concentration or pH. These are some of the areas where surface-enhanced Raman spectroscopy (SERS) can make the most valuable contributions.

SERS circumvents the drawbacks of low signal strength in Raman spectroscopy by relatively simple means. In this method, the greatly enhanced optical fields near a noble metal surface (typically gold or silver) [89, 90] are exploited to enhance the scattering cross-section of the molecular species of interest. In SERS, illumination of the metal surface with the appropriate wavelength of light will cause resonant oscillations of the electron density near the surface of the metal - known as surface plasmons. These surface plasmons create an evanescent field at the metal-air interface, which in addition to charge-transfer and resonant enhancements lead to a significantly enhanced Raman response.

Almost 10 years ago, two groups independently observed Raman scattering from *single* molecules adsorbed to metal nanoparticles [91, 92]. This observation requires 15 orders of magnitude of enhancement in the Raman scattering and, as a result, sparked new interest in understanding the enhancement factors involved in SERS. Recent calculations have shown that at the junction between two nanoparticles separated by 1-3 nm, the E-field enhancement can approach $10^{12}$ [93]. The additional 3 orders of enhancements can then be achieved by charge transfer and resonance Raman effects (most single molecule Raman experiments have been demonstrated with molecules that exhibit significant absorption at or near the wavelengths used in the experiment) [94]. It is, however, still somewhat unclear whether single molecule SERS requires that the molecule has to be in contact with the metal nanostructures to allow for charge transfer and the resulting chemical enhancement or not. Several studies have shown that SERS enhancement is possible without direct analyte to metal contact, but not at the single molecule level [95-98]. A number of observations, such as a concentration-dependent response, the observation of a polarization-dependence of the SERS signal, and later the discovery of on-off variations ("blinking") in the SERS signal intensity strongly indicated that the effect was indeed due to an enhancement of the Raman signature of a single molecule. This extraordinary increase in sensitivity by SERS has even been extended to single biological molecules such as nucleic acids [99] or proteins [100] adsorbed to silver nanoparticles. An additional improvement in signal-to-noise occurs because the conducting nanoparticles tend to quench any natural fluorescence produced by the molecules. Typically, molecules adsorb to the particles by charge-interaction (electrostatics) with the charged nanoparticles or by covalent binding through sulphydril groups (thiolated groups). A major disadvantage of this mechanism, however, is that not every chemical will automatically bind to the particle surface. Thus, most neutral molecules cannot readily be detected by SERS. Also, the Raman spectrum of certain molecules, such as e.g. methanol or water, does not experience any enhancement by SERS, which in many cases is actually a favorable outcome. And, finally, SERS is an extremely localized effect with the enhancement factor decaying within a few nanometers.

Metal nanoparticles can be engineered, deposited, and processed on the nanometer scale in a fairly well-controlled manner, which provides a convenient means for efforts in trying to better control the SERS process. Through recent work with nanoparticles it has become increasingly clear, that specific electromagnetic enhancing sites (e.g. resonant dipole structures) are needed to focus the electric field to small spatial scales [101, 102]. In some special cases, e.g. for silica-gold nanoshells or hollow gold or silver nanospheres, the enhancement effect can also be directed to the entire surface of such an engineered nanoparticle [103, 104]. In this case, the SERS signature is due to an average response of all molecules bound to the surface of the shelled particle rather than a single hot spot or junction, but can be further pronounced by the formation of dimerized particles [102].

The large increase in Raman scattering provided through surface enhancement has significantly extended the range of applications for Raman spectroscopy. Of particular interest are applications in biosensing that directly detect molecular binding events, molecular reactions, or changes in molecular structure due to a change in their local environment [105, 106]. Direct detection of many molecular species works well with SERS, but is problematic, because different chemicals compete for adsorption to the nanoparticle surface and the Raman signature obtained in this case might not always reflect the actual solution concentration of the molecules. Partitioning or conditioning of the surface can often provide higher specificity. An example for recent success in such an area has been the long-standing challenge of detecting glucose by SERS. Glucose by itself does not adsorb to noble metal surfaces. Recently, however, by adsorbing a partioning layer of long-chain alkanes onto the surface of a nanosphere substrate the van Duyne group managed to selectively concentrate glucose within the range of the electromagnetic field enhancement and detect it by SERS [107-109]. This has now even lead to the demonstration of in-vivo glucose sensing [110]. A slightly different approach to sensing with SERS has been demonstrated even earlier and is now gaining significant popularity [106]. SERS particles have been turned into tags with highly multiplexed optical signatures by binding different molecules to the surface of solid nanoparticles and then embedding them in a glass or other biocompatible coating. The molecules, typically different forms of fluorescent dyes, which provide additional resonant Raman enhancement, give off a specific Raman spectrum when probed by laser Raman spectroscopy. Each molecule has a slightly different Raman spectrum and is unique to one type of nanoparticle, so that these tags can now be easily distinguished by their different spectra opening up the possibility to probe hundreds or possibly thousands of particles simultaneously. The surrounding coating makes these particles soluble and inert, and, after functionalizing the particles with antibodies or DNA targets, turns them into highly molecularly specific optical probes. This has been demonstrated by several groups over the last couple of years, which have used this approach to e.g. identify cancer genes, for immunoassays, or to identify viral DNA [111-113]. More recently, because of their brightness, robustness, and highly specific signature, SERS tags have also been used for in-vivo detection of cancer cells in live animals with extremely high sensitivity [114].

Of particular interest for our work is that SERS experiments have shown the technique to be sensitive to subtle changes in molecules attached to the surface of nanoparticles. For example, the SERS responses of mercaptopyridine, mercaptoaniline, and mercaptobenzoic acid have been shown to be sensitive to the pH of the solution surrounding the molecules [115-118]. In addition to the increase in Raman scattering, colloidal silver or gold nanoparticles can also serve as sensitive probes of their local environment [119]. Because the intensity of the electric field decays exponentially with increasing distance from the surface of the metal nanoparticles, the effective sensing region is limited to a few nanometers within the surface of the colloidal particle. These features make SERS particles particularly useful as local sensors that are interesting for monitoring biological processes in vitro and in vivo – even at the level of single cells. Colloidal SERS particles have been incorporated into living cells and were used to measure the prominent chemical species in their local environment [12]. This approach, however, is typically limited to the detection of the most abundant, highly Raman active species or the species with the highest affinity for gold or silver particles. Consequently, we have pursued an approach that focuses on high specificity and also turns SERS-active particles into active chemical probes of their local environment [120]. When the entire surface of SERS particles is coated with the appropriate molecules, the specific Raman response of these probe molecules can be used to monitor changes in the concentration of an analyte while preventing interfering signatures from unspecific binding of other analytes. The general idea is that by attaching "probe" molecules to the nanoparticle surface, changes in the SERS spectrum of the "probe" molecules indicate fluctuations in the concentration of the analyte of interest. This information can be read by monitoring changes in the Raman spectrum in response to chemical binding or conformational changes in the functional groups. This spectroscopic signature, together with the added specificity provided by the functional group results in both, high sensitivity and high chemical specificity.

Our approach has several advantages for cellular level measurements. The spatial resolution afforded by this technique is on diffraction-limited and thus comparable to that achieved with fluorescent dyes. This makes it possible to measure local chemical changes at the subcellular level. Also, because these probes do not rely on electronic transition, as is the case with fluorescent probes, they are extremely robust against photochemical alterations. It is therefore possible to monitor a single particle for extended periods of time without any degradation in the signal. The particle's plasmon resonance is freely adjustable across the optical spectrum. Nanosensors that are resonant in the near-infrared can therefore be probed deep in tissue. Lastly, this approach is readily expandable to provide a wide range of functionalities. For example, boronic acid groups could be used for high affinity for glucose, modifications of EDTA for sensing metal ions, or hydroxyl groups for reactive oxygen species.

### *3.1. pH sensing by SERS*

We have recently demonstrated and applied nanoprobes functionalized with 4-mercaptobenzoic acid as local pH probes [120]. At the level of single cells, fluorescent dyes are typically used as local chemical probes for intra- and intercellular sensing. While fluorescence-based methods for measuring pH in cells and tissues are relatively noninvasive and offer diffraction-limited spatial resolution, they are limited in their capabilities by the need to overcome the cell's intrinsic autofluorescence background, the toxicity of the dyes at higher concentrations, and ultimately by their irreversible photobleaching. Nonetheless, fluorescence detection is currently the method of choice for most high-throughput biological assays and imaging methodologies. Fluorescent indicators are typically based on modifications of the electronic properties of fluorescent dyes. In many cases these dyes are conjugated with functional groups that more or less efficiently quench the dye's fluorescence until it binds to the chemical of interest. Fluorescent dyes have been used to measure intracellular pH both in vitro and in vivo [121-124]. pH sensitive fluorescent dyes are commonly derivatives of fluorescein, which rely on a change in the fluoresence quantum yield as a function of pH [124]. Typically, a ratiometric measurement is used to determine the pH, which corrects for intensity variations that are not due to pH fluctuations. Initially, solid nanoprobes were used for pH sensing, but their heterogeneous size and shape distributions resulted in relatively poor reproducibility of only about 1 pH unit. By engineering uniform hollow nanospheres, we were then able to significantly improve the pH response and reproducibility of the particles. Similar SERS response from single particles [102] and pH detection [125] was recently also shown for nanoshells, i.e. thin metallic shells surrounding a dielectric silica core particle. Intracellular pH-sensitive imaging and hyper-Raman spectroscopy was also demonstrated [126]. Transmission electron micrographs of a solid gold nanoparticle suitable for use as a SERS nanoprobe and a hollow gold nanosphere are shown in Figs. 14a and 14b, respectively. The spectrum in Fig. 14c shows the absorption of a solution of hollow nanospheres with a narrow resonance at ~ 600 nm.

The synthesis of solid and hollow nanospheres was recently described elsewhere [127]. Nanoparticles synthesized by this technique are turned into pH nanoprobes by coating them with 4-mercaptobenzoic acid (4-MBA) to achieve monolayer surface coverage. To 1 mL nanospheres in aqueous solution, 50 µl of a saturated 4-mercaptobenzoic acid solution in ethanol is added. After incubation for 1h, the nanosphere solution is centrifuged for 10 min. at 13,000 rpm and then washed 3 times in PBS. 4-MBA provides a pH response through its SERS spectrum right in the physiologically interesting pH range [104, 120]. This is illustrated in Fig. 15a, which displays the characteristic SERS spectra obtained from hollow silver nanoparticles coated with 4-MBA. The characteristic feature in these spectra is the absence of a $COO^-$ stretching mode near 1400 $cm^{-1}$ at low pH when the carboxylic acid group of 4-MBA is protonated and a strong peak near 1400 $cm^{-1}$ at higher pH when the majority of carboxylic acid groups are deprotonated. When the intensity of this or other pH sensitive stretching modes are normalized to a pH insensitive stretching mode and plotted against the pH of the bulk solution, a characteristic pH titration curve can be obtained.

There are several unique features of these SERS probes that make them well-suited for nanoscale pH measurements. First, the apparent $pK_a$ of approximately 6.5 for 4-MBA is significantly more alkaline than that of pure benzoic acid ($pK_a$ = 4.20). This is likely the result of both conjugation to the nanoparticle and the ionic strength of the buffer solution and in the present case works in our favor. Also, the SERS spectra shown in Fig. 15a were obtained in a custom-built confocal microcope that uses a red helium-neon laser (632.8 nm wavelength) as excitation source. At this wavelength, contributions from background fluorescence are minimal. These particles are highly resistant against photodecomposition when probed outside the resonant absorption of the probe molecules, but in resonance with the surface plasmons supported by the nanoparticle surface. This is demonstrated in Fig. 15b, where a single pH active nanoparticle was probed under continuous illumination at 632.8 nm excitation. The spectrum is reproduced over the entire 20 minutes without signal degradation. Only fluctuations of the overall spectral intensity are observed, which are due to intensity fluctuations of the Helium-Neon laser that was used to probe the nanoparticle.

An advantage of gold nanoprobes is that despite their small size they can easily be visualized by darkfield microscopy or video-enhanced differential interference contrast (DIC) microscopy - even against the background of a cell or tissue section. These particles scatter light very efficiently and are many orders of magnitude brighter than fluorescent molecules. As demonstrated in Fig. 16, we have demonstrated this by imaging gold nanoparticles after their incorporation into cells. The sequence of darkfield images in this figure shows 60 nm gold nanoparticles diffusing in the interior of bovine endothelial cells. Here, the nanoparticles were functionalized with the protein transduction domain of the HIV virus, the TAT peptide. This highly charged peptide inserts itself into the membrane of cells and causes the cells to uptake the nanoparticles resulting in their confinement to the interior of the cells. The series of images in Fig. 16 demonstrates this for the particles highlighted by the white circle. Incorporating nanoparticles into cells by uptake peptides, however, usually results in a severe cellular response or localization of the particles in endosomes, which leads us to continue searching for other, alternative cell delivery approaches.

## Conclusions

In this review paper we have discussed and compared different approaches to the nondestructive analysis and imaging of single cells by Raman spectroscopy which provide chemical information about cells optimized to specific applications. Spontaneous Raman spectroscopy continues to be a powerful technique for the biochemical analysis of living cells and, in conjunction with laser tweezers, subcellular particles as well. It can be broadly applied to a wide range of biomedical problems such as cancer, infectious disease, cardiovascular disease, and regenerative medicine, to name a few, for identifying and sorting different cell phenotypes and discriminating between different cell populations. The prospect of developing Raman spectroscopy as a new capability for flow cytometry and cell sorting[128] and incorporating it into existing cytometers is foreseeable in the future, since the field of flow cytometry is constantly seeking new parameters that can be simultaneously measured on the cellular level. In order for this technology to be fully utilized by cell biologists, however, some improvements need to be made to increase the sampling rate and the size of the cell populations to be analyzed. The design and fabrication of microfluidic devices applicable to Raman spectroscopy for automated cell delivery to the laser trap is expected to be a major component of this technology, as well as the development of nonlinear Raman spectroscopy combined with optical tweezers[129, 130] for more rapid, label-free spectral analysis of single cells.

A faster and more sensitive approach to single cell Raman imaging is provided by CARS microscopy. CARS imaging has seen rapid growth and adoption in materials science, chemistry, and biology over the last couple of years. Although video rate CARS imaging has already been demonstrated in vivo, the limits on these imaging rates will continue to be pushed to provide CARS imaging methods capable of monitoring faster dynamics of biological systems in three dimensions. Its combination with endoscopy will open it up to the biomedical community for applications such as the label-free inspection of the epithelial cell layer, cardiovascular imaging, and tumor demarcation. Key, here, will be the prospect of making CARS systems available to a wider range of researchers without the cost being prohibitively expensive and its operation fraught with complexity. The development of compact laser sources capable of fiber delivery, as well as affordable commercial turnkey CARS imaging systems, will greatly aid in this goal. Other obstacles, such as increasing the imaging depth and field of view also still need to yet be overcome. The sensitivity of CARS microscopy through efficient rejection of the non-resonant background will continue to be pushed, especially if imaging at Raman modes other than the aliphatic C-H mode is desired. Broadband CARS techniques that rapidly provide full spectral information, novel Raman imaging probes, as well as the development of alternative techniques, such as stimulated Raman scattering (SRS) microscopy have significant prospects in these areas.

Surface-enhanced Raman spectroscopy is yet another mechanism to overcome the weak signals obtained from Raman scattering. SERS nanosensors such as the pH-sensitive particles that we discussed have a similar spectroscopic signature as SERS tags, which have recently been shown to provide superior sensitivity for in-vivo experiments. Nanosensors have the added benefit that they are "active", i.e. their signature changes according to changes in their local environment, e.g. binding events. This property is expected to work just as well for deep tissue imaging in-vivo. Other applications are expected from the use of bioactive nanoprobes that might be able to e.g. detect post-translational protein modifications in-vivo [131]. Additional benefits might arise from the combination of SERS nanoprobes with CARS microscopy, which should provide superior bleaching-resistant sensitivity for in-vivo sensing compared to any other optical probe.

The improvements made in sensitivity, microscopy and spectroscopy schemes, as well as in novel surface-enhancing nanomaterials and structures have demonstrated that Raman spectroscopy and microscopy provides valuable information even at the level of single living cells. Raman spectroscopy is a powerful analysis technique in its own right or as part of multi-modality analyses e.g. in conjunction with traditional optical microscopy. A number of commercial implementations with high sensitivity are already available and more will become available in the very near future, opening this technique up to biologists and biomedical researchers with no background in advanced optical spectroscopy.

## Acknowledgements

We would like to thank our colleagues and collaborators who have provided us with materials, samples, and many illuminating discussions over the last couple of years. Specifically, we would like to thank Chad Talley, Christopher Hollars, Adam Schwartzberg, Stephen Lane, Leonard Jusinski, Heiko Winhold, Ted Laurence, Rod Balhorn, Monique Cosman, Douglas Taylor, Tammy Olson, Christine Orme, Jin Zhang, John Rutledge, Juliana Sampson, Gregory McNerney, Tyler Weeks, Sonny Ly, Iwan Schie, J. Clark Lagarias, Yi-Shin Sun, Theodore Zwerdling, Naomi Halas, Peter Nordlander, and Chris Pivetti. This work was supported in part by funding from the National Science Foundation. The Center for Biophotonics, an NSF Science and Technology Center, is managed by the University of California, Davis, under Cooperative Agreement No. PHY 0120999. T. Huser also acknowledges support by the Clinical Translational Science Center under grant number UL1 RR024146 from the National Center for Research Resources (NCRR), a component of the National Institutes of Health (NIH), and the NIH Roadmap for Medical Research. J.W. Chan acknowledges support from the LLNL Laboratory-directed Research and Development Program. Work at LLNL was performed under the auspices of the U.S. Department of Energy by Lawrence Livermore National Laboratory under Contract DE-AC52-07NA27344.

## References

1. Raman, C.V. and K.S. Krishnan, *A new type of secondary radiation.* Nature, 1928. 121: p. 501-502.
2. Chan, J.W., et al., *Micro-Raman spectroscopy detects individual neoplastic and normal hematopoietic cells.* Biophysical Journal, 2006. 90(2): p. 648-656.
3. Matousek, P., et al., *Fluorescence suppression in resonance Raman spectroscopy using a high-performance picosecond Kerr gate.* Journal of Raman Spectroscopy, 2001. 32(12): p. 983-988.
4. Matousek, P., et al., *Efficient rejection of fluorescence from Raman spectra using picosecond Kerr gating.* Applied Spectroscopy, 1999. 53(12): p. 1485-1489.
5. Wood, B.R., et al., *Resonance Raman spectroscopy of red blood cells using near-infrared laser excitation.* Analytical and Bioanalytical Chemistry, 2007. 387(5): p. 1691-1703.
6. Wood, B.R., L. Hammer, and D. McNaughton, *Resonance Raman spectroscopy provides evidence of heme ordering within the functional erythrocyte.* Vibrational Spectroscopy, 2005. 38(1-2): p. 71-78.
7. Ramser, K., et al., *Resonance Raman spectroscopy of optically trapped functional erythrocytes.* Journal of Biomedical Optics, 2004. 9(3): p. 593-600.
8. Yazdi, Y., et al., *Resonance Raman spectroscopy at 257 nm excitation of normal and malignant cultured breast and cervical cells.* Applied Spectroscopy, 1999. 53(1): p. 82-85.
9. Duncan, M.D., J. Reintjes, and T.J. Manuccia, *Scanning Coherent Anti-Stokes Raman Microscope.* Optics Letters, 1982. 7(8): p. 350-352.
10. Zumbusch, A., G.R. Holtom, and X.S. Xie, *Three-dimensional vibrational imaging by coherent anti-Stokes Raman scattering.* Physical Review Letters, 1999. 82(20): p. 4142-4145.
11. Jeanmaire, D.L. and R.P. Vanduyne, *Surface Raman Spectroelectrochemistry .1. Heterocyclic, Aromatic, and Aliphatic-Amines Adsorbed on Anodized Silver Electrode.* Journal of Electroanalytical Chemistry, 1977. 84(1): p. 1-20.
12. Kneipp, K., et al., *Surface-enhanced Raman Spectroscopy in single living cells using gold nanoparticles.* Applied Spectroscopy, 2002. 56(2): p. 150-154.
13. Kneipp, K., et al., *Population pumping of excited vibrational states by spontaneous surface-enhanced Raman scattering.* Physical Review Letters, 1996. 76(14): p. 2444-2447.
14. Moskovits, M., *Surface-Enhanced Spectroscopy.* Reviews of Modern Physics, 1985. 57(3): p. 783-826.
15. Puppels, G.J., et al., *Studying Single Living Cells and Chromosomes by Confocal Raman Microspectroscopy.* Nature, 1990. 347(6290): p. 301-303.
16. Maquelin, K., et al., *Identification of medically relevant microorganisms by vibrational spectroscopy.* Journal of Microbiological Methods, 2002. 51(3): p. 255-271.
17. Maquelin, K., et al., *Rapid identification of Candida species by confocal Raman micro spectroscopy.* Journal of Clinical Microbiology, 2002. 40(2): p. 594-600.
18. Maquelin, K., et al., *Rapid epidemiological analysis of Acinetobacter strains by Raman spectroscopy.* Journal of Microbiological Methods, 2006. 64(1): p. 126-131.
19. de Jong, B.W.D., et al., *Discrimination between nontumor bladder tissue and tumor by Raman spectroscopy.* Analytical Chemistry, 2006. 78(22): p. 7761-7769.
20. Taleb, A., et al., *Raman microscopy for the chemometric analysis of tumor cells.* Journal of Physical Chemistry B, 2006. 110(39): p. 19625-19631.
21. Chen, K., et al., *Diagnosis of colorectal cancer using Raman spectroscopy of laser-trapped single living epithelial cells.* Optics Letters, 2006. 31(13): p. 2015-2017.
22. Buschman, H.P., et al., *Diagnosis of human coronary atherosclerosis by morphology-based Raman spectroscopy.* Cardiovascular Pathology, 2001. 10(2): p. 59-68.
23. van de Poll, S.W.E., et al., *In situ investigation of the chemical composition of ceroid in human atherosclerosis by Raman spectroscopy.* Journal of Raman Spectroscopy, 2002. 33(7): p. 544-551.

24. Silveira, L., et al., *Near-infrared raman spectroscopy of human coronary arteries: Histopathological classification based on mahalanobis distance.* Journal of Clinical Laser Medicine & Surgery, 2003. 21(4): p. 203-208.

25. Uzunbajakava, N., et al., *Nonresonant confocal Raman imaging of DNA and protein distribution in apoptotic cells.* Biophysical Journal, 2003. 84(6): p. 3968-3981.

26. Uzunbajakava, N., et al., *Nonresonant Raman imaging of protein distribution in single human cells.* Biopolymers, 2003. 72(1): p. 1-9.

27. Huang, Y.S., et al., *Raman spectroscopic signature of life in a living yeast cell.* Journal of Raman Spectroscopy, 2004. 35(7): p. 525-+.

28. Huang, Y.S., et al., *Molecular-level investigation of the structure, transformation, and bioactivity of single living fission yeast cells by time- and space-resolved Raman spectroscopy.* Biochemistry, 2005. 44(30): p. 10009-10019.

29. Naito, Y., A. Toh-e, and H.O. Hamaguchi, *In vivo time-resolved Raman imaging of a spontaneous death process of a single budding yeast cell.* Journal of Raman Spectroscopy, 2005. 36(9): p. 837-839.

30. de Grauw, C.J., C. Otto, and J. Greve, *Line-scan Raman microspectrometry for biological applications.* Applied Spectroscopy, 1997. 51(11): p. 1607-1612.

31. Otto, C., et al., *Applications of micro-Raman imaging in biomedical research.* Journal of Raman Spectroscopy, 1997. 28(2-3): p. 143-150.

32. Xie, C.G., M.A. Dinno, and Y.Q. Li, *Near-infrared Raman spectroscopy of single optically trapped biological cells.* Optics Letters, 2002. 27(4): p. 249-251.

33. Xie, C.G. and Y.Q. Li, *Cohfocal micro-Raman spectroscopy of single biological cells using optical trapping and shifted excitation difference techniques.* Journal of Applied Physics, 2003. 93(5): p. 2982-2986.

34. Chan, J.W., et al., *Reagentless identification of single bacterial spores in aqueous solution by confocal laser tweezers Raman spectroscopy.* Analytical Chemistry, 2004. 76(3): p. 599-603.

35. Xie, C.G., et al., *Real-time Raman spectroscopy of optically trapped living cells and organelles.* Optics Express, 2004. 12(25): p. 6208-6214.

36. Creely, C.M., G.P. Singh, and D. Petrov, *Dual wavelength optical tweezers for confocal Raman spectroscopy.* Optics Communications, 2005. 245(1-6): p. 465-470.

37. Ashkin, A., *Applications of Laser Radiation Pressure.* Science, 1980. 210(4474): p. 1081-1088.

38. Ashkin, A., J.M. Dziedzic, and T. Yamane, *Optical trapping and manipulation of single cells using infrared laser beams.* Nature, 1987. 330(6150): p. 769-71.

39. Jess, P., et al., *A dual beam fibre trap for Raman microspectroscopy of single cells.* Optics Express, 2006. 14: p. 5779-5791

40. Chan, J.W., et al., *Raman spectroscopic analysis of biochemical changes in individual triglyceride-rich lipoproteins in the pre- and postprandial state.* Analytical Chemistry, 2005. 77(18): p. 5870-5876.

41. Chan, J.W., et al., *Monitoring dynamic protein expression in living E-coli. Bacterial Celts by laser tweezers raman spectroscopy.* Cytometry Part A, 2007. 71A(7): p. 468-474.

42. Xie, C.G., et al., *Detection of the recombinant proteins in single transgenic microbial cell using laser tweezers and Raman Spectroscopy.* Analytical Chemistry, 2007. 79(24): p. 9269-9275.

43. Singh, G.P., et al., *The lag phase and G(1) phase of a single yeast cell monitored by Raman microspectroscopy.* Journal of Raman Spectroscopy, 2006. 37(8): p. 858-864.

44. Chen, D., S.S. Huang, and Y.Q. Li, *Real-time detection of kinetic germination and heterogeneity of single Bacillus spores by laser tweezers Raman spectroscopy.* Analytical Chemistry, 2006. 78(19): p. 6936-6941.

45. Singh, G.P., et al., *Real-time detection of hyperosmotic stress response in optically trapped single yeast cells using Raman microspectroscopy.* Analytical Chemistry, 2005. 77(8): p. 2564-2568.
46. Mannie, M.D., et al., *Activation-dependent phases of T cells distinguished by use of optical tweezers and near infrared Raman spectroscopy.* Journal of Immunological Methods, 2005. 297(1-2): p. 53-60.
47. Deng, J.L., et al., *Study of the effect of alcohol on single human red blood cells using near-infrared laser tweezers Raman spectroscopy.* Journal of Raman Spectroscopy, 2005. 36(3): p. 257-261.
48. Crane, N.J., et al., *Raman imaging demonstrates FGF2-induced craniosynostosis in mouse calvaria.* Journal of Biomedical Optics, 2005. 10(3): p. 8.
49. Kazanci, M., et al., *Raman imaging of two orthogonal planes within cortical bone.* Bone, 2007. 41(3): p. 456-461.
50. Zhang, G.J., et al., *Vibrational microscopy and imaging of skin: from single cells to intact tissue.* Analytical and Bioanalytical Chemistry, 2007. 387(5): p. 1591-1599.
51. Zhang, G.J., et al., *Imaging the prodrug-to-drug transformation of a 5-fluorouracil derivative in skin by confocal Raman microscopy.* Journal of Investigative Dermatology, 2007. 127(5): p. 1205-1209.
52. Burkacky, O., et al., *Dual-pump coherent anti-Stokes-Raman scattering microscopy.* Optics Letters, 2006. 31(24): p. 3656-3658.
53. Cheng, J.X., *Coherent anti-Stokes Raman Scatteriong microscopy.* Applied Spectroscopy, 2007. 61(9): p. 197A-208A.
54. Cheng, J.X., et al., *Laser-scanning coherent anti-stokes Raman scattering microscopy and applications to cell biology.* Biophysical Journal, 2002. 83(1): p. 502-509.
55. Cheng, J.X., A. Volkmer, and X.S. Xie, *Theoretical and experimental characterization of coherent anti-Stokes Raman scattering microscopy.* Journal of the Optical Society of America B-Optical Physics, 2002. 19(6): p. 1363-1375.
56. Cheng, J.X. and X.S. Xie, *Coherent anti-Stokes Raman scattering microscopy: Instrumentation, theory, and applications.* Journal of Physical Chemistry B, 2004. 108(3): p. 827-840.
57. Djaker, N., et al., *Coherent anti-Stokes Raman scattering microscopy (CARS): Instrumentation and applications.* Nuclear Instruments & Methods in Physics Research Section a-Accelerators Spectrometers Detectors and Associated Equipment, 2007. 571(1-2): p. 177-181.
58. Evans, C.L., et al., *Chemical imaging of tissue in vivo with video-rate coherent anti-Stokes Raman scattering microscopy.* Proceedings of the National Academy of Sciences of the United States of America, 2005. 102(46): p. 16807-16812.
59. Huff, T.B. and J.X. Cheng, *In vivo coherent anti-Stokes Raman scattering imaging of sciatic nerve tissue.* Journal of Microscopy-Oxford, 2007. 225(2): p. 175-182.
60. Kano, H. and H. Hamaguchi, *Vibrationally resonant imaging of a single living cell by supercontinuum-based multiplex coherent anti-Stokes Raman scattering microspectroscopy.* Optics Express, 2005. 13(4): p. 1322-1327.
61. Muller, M. and A. Zumbusch, *Coherent anti-stokes Raman scattering microscopy.* Chemphyschem, 2007. 8(15): p. 2157-2170.
62. Nan, X.L., E.O. Potma, and X.S. Xie, *Nonperturbative chemical imaging of organelle transport in living cells with coherent anti-stokes Raman scattering microscopy.* Biophysical Journal, 2006. 91(2): p. 728-735.
63. Rodriguez, L.G., S.J. Lockett, and G.R. Holtom, *Coherent anti-stokes Raman scattering microscopy: A biological review.* Cytometry Part A, 2006. 69A(8): p. 779-791.
64. Tong, L., et al., *Imaging receptor-mediated endocytosis with a polymeric nanoparticle-based coherent anti-stokes raman scattering probe.* Journal of Physical Chemistry B, 2007. 111(33): p. 9980-9985.

65. Volkmer, A., J.X. Cheng, and X.S. Xie, *Vibrational imaging with high sensitivity via epidetected coherent anti-Stokes Raman scattering microscopy.* Physical Review Letters, 2001. 8702(2): p. 4.
66. Wang, H.F., et al., *Coherent anti-stokes Raman scattering imaging of axonal myelin in live spinal tissues.* Biophysical Journal, 2005. 89(1): p. 581-591.
67. Cheng, J.X., et al., *An epi-detected coherent anti-stokes raman scattering (E-CARS) microscope with high spectral resolution and high sensitivity.* Journal of Physical Chemistry B, 2001. 105(7): p. 1277-1280.
68. Hashimoto, M. and T. Araki, *Molecular vibration imaging in the fingerprint region by use of coherent anti-Stokes Raman scattering microscopy with a collinear configuration.* Optics Letters, 2000. 25(24): p. 1768-1770.
69. Lee, E.S., J.Y. Lee, and Y.S. Yoo, *Nonlinear optical interference of two successive coherent anti-Stokes Raman scattering signals for biological imaging applications.* Journal of Biomedical Optics, 2007. 12(2): p. 5.
70. Potma, E.O., C.L. Evans, and X.S. Xie, *Heterodyne coherent anti-Stokes Raman scattering (CARS) imaging.* Optics Letters, 2006. 31(2): p. 241-243.
71. Toytman, I., et al., *Wide-field coherent anti-Stokes Raman scattering microscopy with non-phase-matching illumination.* Optics Letters, 2007. 32(13): p. 1941-1943.
72. Fu, Y., et al., *Characterization of photodamage in coherent anti-Stokes Raman scattering microscopy.* Optics Express, 2006. 14(9): p. 3942-3951.
73. Ganikhanov, F., et al., *Broadly tunable dual-wavelength light source for coherent anti-Stokes Raman scattering microscopy.* Optics Letters, 2006. 31(9): p. 1292-1294.
74. Fu, Y., et al., *Second harmonic and sum frequency generation imaging of fibrous astroglial filaments in ex vivo spinal tissues.* Biophysical Journal, 2007. 92(9): p. 3251-3259.
75. Le, T.T., et al., *Label-free molecular imaging of atherosclerotic lesions using multimodal nonlinear optical microscopy.* Journal of Biomedical Optics, 2007. 12(5): p. 10.
76. Cheng, J.X., L.D. Book, and X.S. Xie, *Polarization coherent anti-Stokes Raman scattering microscopy.* Optics Letters, 2001. 26(17): p. 1341-1343.
77. Volkmer, A., L.D. Book, and X.S. Xie, *Time-resolved coherent anti-Stokes Raman scattering microscopy: Imaging based on Raman free induction decay.* Applied Physics Letters, 2002. 80(9): p. 1505-1507.
78. von Vacano, B. and M. Motzkus, *Time-resolved two color single-beam CARS employing supercontinuum and femtosecond pulse shaping.* Optics Communications, 2006. 264(2): p. 488-493.
79. Ganikhanov, F., et al., *High-sensitivity vibrational imaging with frequency modulation coherent anti-Stokes Raman scattering (FM CARS) microscopy.* Optics Letters, 2006. 31(12): p. 1872-1874.
80. Schie, I.W., et al., *Simultaneous forward and epi-CARS microscopy with a single detector by time-correlated single photon counting.* Optics Express, 2008. 16(3): p. 2168-2175.
81. Becker, W., et al., *Fluorescence lifetime imaging by time-correlated single-photon counting.* Microscopy Research and Technique, 2004. 63(1): p. 58-66.
82. Duncan, R.R., et al., *Multi-dimensional time-correlated single photon counting (TCSPC) fluorescence lifetime imaging microscopy (FLIM) to detect FRET in cells.* Journal of Microscopy-Oxford, 2004. 215: p. 1-12.
83. Peter, M. and S.M. Ameer-Beg, *Imaging molecular interactions by multiphoton FLIM.* Biology of the Cell, 2004. 96(3): p. 231-236.
84. Suhling, K., P.M.W. French, and D. Phillips, *Time-resolved fluorescence microscopy.* Photochemical & Photobiological Sciences, 2005. 4(1): p. 13-22.
85. Kraemer, B., et al., *Time-resolved laser scanning microscopy with FLIM and advanced FCS capability.* Proceedings of SPIE, 2005. 5700: p. 138-143.

86. Elson, D., et al., *Fluorescence lifetime system for microscopy and multiwell plate imaging with a blue picosecond diode laser* Optics Letters, 2002. 27(1409 - 1411).

87. Wahl, M., et al., *Dead-time optimized time-correlated photon counting instrument with synchronized, independent timing channels* Review of Scientific Instruments, 2007. 78: p. 033106.

88. Ly, S., et al., *Time-gated single photon counting enables separation of CARS microscopy data from multiphoton-excited tissue autofluorescence.* Optics Express, 2007. 15(25): p. 16839-16851.

89. Kneipp, K., et al., *Ultrasensitive chemical analysis by Raman spectroscopy.* Chemical Reviews, 1999. 99(10): p. 2957-2975,COVER4.

90. Kneipp, K., et al., *Surface-Enhanced Raman Scattering in Biophysics.* J. Phys.: Condens. Matter, 2002. 14: p. R597-R624.

91. Nie, S. and S.R. Emory, *Probing Single Molecules and Single Nanoparticles by Surface-Enhanced Raman Scattering.* Science, 1997. 275: p. 1102-1106.

92. Kneipp, K., et al., *Single Molecule Detection Using Surface-Enhanced Raman Scattering (SERS).* Phys. Rev. Lett., 1997. 78(9): p. 1667-1670.

93. Xu, H., et al., *Electromagnetic Contributions to Single-Molecule Sensitivity in Surface-Enhanced Raman Scattering.* Phys. Rev. E., 2000. 62(3): p. 4318-4324.

94. Kneipp, K., et al., *Ultrasensitive Chemical Analysis by Raman Spectroscopy.* Chem. Rev., 1999. 99: p. 2957-2975.

95. Murray, C.A., D.L. Allara, and M. Rhinewine, *Silver-Molecule Separation Dependence of Surface-Enhanced Raman Scattering.* Phys. Rev. Lett., 1980. 46(1): p. 57-60.

96. Murray, C.A. and D.L. Allara, *Measurement of the Molecule-Silver Separation Dependence of Surface Enhanced Raman Scattering in Multilayered Structures.* J. Chem. Phys., 1982. 76(3): p. 1290-1303.

97. Ye, Q., J. Fang, and L. Sun, *Surface-Enhanced Raman Scattering from Functionalized Self-Assembled Monolayers. 2. Distance Dependence of Enhanced Raman Scattering from an Azobenzene Terminal Group.* J. Phys. Chem. B, 1997. 101: p. 8221-8224.

98. Kennedy, B.J., et al., *Determination of the Distance Dependence and Experimental Effects for Modified SERS Substrates Based on Self-Assembled Monolayers Formed Using Alkanethiols.* J. Phys. Chem. B, 1999. 103: p. 3640-3646.

99. Kneipp, K., et al., *Detection and identification of a single DNA base molecule using surface-enhanced Raman scattering (SERS).* Physical Review E, 1998. 57(6): p. R6281-R6284.

100. Xu, H., et al., *Spectroscopy of single Hemoglobin molecules by surface enhanced Raman scattering.* Physical Review Letters, 1999. 83(21): p. 4357-4360.

101. Michaels, A.M., J. Jiang, and L.E. Brus, *Ag Nanocrystal Junctions as the Site for Surface-Enhanced Raman Scattering of Single Rhodamine 6G Molecules.* J. Phys. Chem. B, 2000. 104: p. 11965-11971.

102. Talley, C.E., et al., *Surface-enhanced Raman Scattering from Individual Au Nanoparticles and Nanoparticle Dimer Substrates.* Nano Letters, 2005. 5(8): p. 1569-1574

103. Jackson, J. and N. Halas, *Surface-enhanced Raman scattering on tunable plasmonic nanoparticle substrates.* Proc. Natl. Acad. Sci. USA, 2004. 101: p. 17930-17935.

104. Schwartzberg, A.M., et al., *Improving nanoprobes using surface-enhanced Raman scattering from 30-nm hollow gold particles.* Analytical Chemistry, 2006. 78(13): p. 4732-4736.

105. Haynes, C.L., A.D. McFarland, and R.P. Van Duyne, *Surface-Enhanced Raman Spectroscopy.* Analytical Chemistry, 2005. 77: p. 338A-346A.

106. Vo-Dinh, T., F. Yan, and M.B. Wabuyele, *Surface-enhanced Raman scattering for medical diagnostics and biological imaging.* Journal of Raman Spectroscopy, 2005. 36: p. 640-647.

107. Lyandres, O., et al., *Real-time glucose sensing by surface-enhanced Raman spectroscopy in bovine plasma facilitated by a mixed decanethiol/mercaptohexanol partition layer.* Anal Chem, 2005. 77(19): p. 6134-9.

108. Stuart, D.A., et al., *Glucose sensing using near-infrared surface-enhanced Raman spectroscopy: gold surfaces, 10-day stability, and improved accuracy.* Anal Chem, 2005. 77(13): p. 4013-9.

109. Yonzon, C.R., et al., *A glucose biosensor based on surface-enhanced Raman scattering: improved partition layer, temporal stability, reversibility, and resistance to serum protein interference.* Anal Chem, 2004. 76(1): p. 78-85.

110. Stuart, D.A., et al., *In vivo glucose measurement by surface-enhanced Raman spectroscopy.* Anal Chem, 2006. 78(20): p. 7211-5.

111. Vo-Dinh, T., L.R. Allain, and D.L. Stokes, *Cancer gene detection using surface-enhanced Raman scattering (SERS)* Journal of Raman Spectroscopy, 2002. 33: p. 511-516.

112. Allain, L.R. and T. Vo-Dinh, *Surface-enhanced Raman scattering detection of the breast cancer susceptibility gene BRCA1 using a silver-coated microarray platform.* Analytica Chimica Acta, 2002. 469 p. 149-154.

113. Cao, Y.C., R. Jin, and C.A. Mirkin, *Nanoparticles with Raman spectroscopic fingerprints for DNA and RNA detection* Science, 2002. 297: p. 1536-1540.

114. Qian, X.M., et al., *In vivo tumor targeting and spectroscopic detection with surface-enhanced Raman nanoparticle tags* Nature Biotechnology, 2008. 26: p. 83-90.

115. Lee, S.B., K. Kim, and M.S. Kim, *Surface-Enhanced Raman Scattering of o-Mercaptobenzoic Acid in Silver Sol.* J. Raman Spectrosc., 1991. 22: p. 811-817.

116. Hill, W. and B. Wehling, *Potential- and pH-Dependent Surface-Enhanced Raman Scattering of p-Mercaptoaniline on Silver and Gold Substrates.* J. Phys. Chem., 1993. 97: p. 9451-9455.

117. Yu, H.-Z., N. Xia, and Z.-F. Liu, *SERS Titration of 4-Mercaptopyridine Self-Assembled Monolayers at Aqueous Buffer/Gold Interfaces.* Anal. Chem., 1999. 71: p. 1354-1358.

118. Michota, A. and J. Bukowska, *Surface-Enhanced Raman Scattering (SERS) of 4-Mercaptobenzoic Acid on Silver and Gold Substrates.* J. Raman Spectrosc., 2003. 34: p. 21-25.

119. Zeiri, L., et al., *Silver metal induced surface enhanced Raman of bacteria.* Colloids and Surfaces a-Physicochemical and Engineering Aspects, 2002. 208(1-3): p. 357-362.

120. Talley, C.E., et al., *Intracellular pH sensors based on surface-enhanced Raman scattering.* Analytical Chemistry, 2004. 76(23): p. 7064-7068.

121. Helmlinger, G., et al., *Acid Production in Glycolysis-impaired Tumors Provides New Insights into Tumor Metabolism.* Clin. Cancer Res., 2002. 8: p. 1284-1291.

122. Ishaque, A. and M. Al-Rubeai, *Use of intracellular pH and annexin-V flow cytometric assays to monitor apoptosis and its suppression by bcl-2 over-expression in hybridoma cell culture.* J. Immunol. Methods, 1998. 221: p. 43-57.

123. Xu, L., D. Fukumura, and R.K. Jain, *Acidic Extracellular pH Induces Vascular Endothelial Growth Facter (VEGF) in Human Glioblastoma Cells via ERK1/2 MAPK Signaling Pathway.* J. Biol. Chem., 2002. 277(13): p. 11368-11374.

124. Haugland, R.P., in *Handbook of Fluorescent Probes and Research Products*. 2002, Molecular Probes, Inc. p. 829-840.

125. Bishnoi, S.W., et al., *All-optical nanoscale pH meter.* Nano Letters, 2006. 6: p. 1687-1692

126. Kneipp, J., et al., *One- and two-photon excited optical ph probing for cells using surface-enhanced Raman and hyper-Raman nanosensors.* Nano Lett, 2007. 7(9): p. 2819-23.

127. Schwartzberg, A.M., et al., *Synthesis, characterization, and tunable optical properties of hollow gold nanospheres.* J Phys Chem B, 2006. 110(40): p. 19935-44.

128. Jett, J.H., *Raman spectroscopy comes to flow Cytometry.* Cytometry Part A, 2008. 73A(2): p. 109-110.

129. Shi, K.B., P. Li, and Z.W. Liu, *Supercontinuum cars tweezers.* Journal of Nonlinear Optical Physics & Materials, 2007. 16(4): p. 457-470.

130. Chan, J.W., et al., *Optical trapping and coherent anti-Stokes Raman scattering (CARS) spectroscopy of submicron-size particles.* IEEE Journal of Selected Topics in Quantum Electronics, 2005. 11(4): p. 858-863.
131. Sundararajan, N., et al., *Ultrasensitive detection and characterization of posttranslational modifications using surface-enhanced Raman spectroscopy.* Analytical Chemistry, 2006. 78: p. 3543-3550.

## Figure Captions

**Figure 1:** Top: schematic of the Raman process, showing the incident photons characterized by the energy $E_i$ and frequency $\nu_i$, and the Raman scattered photons characterized by the energy $E_s$ and frequency $\nu_s$. h represents Planck's constant. Bottom: Jablonsky diagram of the main Raman processes described in the text. $S_0$ and $S_1$ represent the ground and first excited electronic singlet states, while vibrational states drawn on top of the electronic states are denoted with 0, 1, 2, and 3.

**Figure 2:** (a) Typical representation of spontaneous Stokes (to the right of the laser line) and anti-Stokes (to the left of the laser line) Raman scattering spectra. (b) Diagram showing enhancement of anti-Stokes Raman scattering when the difference between the energies of the pump and Stokes lasers matches the energy of a Raman vibration.

**Figure 3:** General layout of a Raman imaging setup.

**Figure 4:** (a) Schematic illustration of a confocal Raman microscope. L – Continuous wave laser, BP – bandpass filter, DM – dichroic mirror, MO – microscope objective, S – scan stage, SF – spatial filter, LP – longpass filter, SP – spectrometer, G – blazed grating, CCD – thermoelectrically cooled CCD detector (b) Brightfield and fluorescence image of a live, Hoechst dye-stained monocyte. Fluorescence signals from the DNA targeting dye are observed primarily within the nucleus. Point Raman spectra of the nuclear and cytoplasmic regions within the cell show spectral differences reflecting the relative amounts of DNA and Hoechst dye.

**Figure 5:** Comparison of the point and line scanning methods for Raman imaging. Point scanning illuminates the sample with a single spot to acquire a single Raman spectrum. Point scanning requires two dimensional scanning to generate a Raman image. Conversely, line scanning illuminates the sample with a line that is imaged through the slit, resulting in the collecting of multiple spectra along the line. Therefore, line illumination only requires scanning along one axis, allowing for faster imaging.

**Figure 6:** (a) Ray optics illustration of the lateral forces imparted on a particle exposed to a laser trap by the transfer of photon momentum to the particle (b) A particle within the laser focus of an optical trap is subjected to multiple forces in both the lateral and axial directions.

**Figure 7:** Different optical configurations for a laser tweezers Raman spectroscopy system (a) a single laser or collinear dual laser beam optical trap (b) a dual beam counter-propagating laser trap (c) a dual fiber coupled laser trap with a Raman probe beam normal to the fiber axis.

**Figure 8:** Summary of the different types of individual biological particles that have been trapped and analyzed in our group. Shown are representative images and spectra of the different samples. (a) Sub-micron sized particles such as cell organelles and lipid particles (b) Micron sized particles such as bacterial spores and micro-organisms (c) Single cells such as human sperm and lymphocytes

**Figure 9:** (a) Mean Raman spectra of normal T lymphocytes, transformed Jurkat T cells, and isolated cancer T cells from a leukemia patient. Highlighted in gray are Raman markers that are noticeably different between the normal and cancer/transformed cell groups (see text and references). (b) Difference spectra obtained by subtracting the normal T cell spectra from the transformed Jurkat T cell and leukemia T cell spectra to highlight the major spectral differences. (c) PCA plots of the first two principal components show separation between the normal T cell group and the transformed Jurkat T / leukemic T cell groups.

**Figure 10:** (a) Simplified layout of a typical CARS microscopy system used in our laboratory. Pump and probe laser beams are overlapped in time and space, then coupled into an optical microscope with a microscope objective with high numerical aperture. CARS signals are detected spectroscopically or with a point detector. Abbreviations: BS beam splitter, DM dichroic mirror, PP pulse picker, OPO optical parametric oscillator, BE beam expander, OL objective lens, SP short pass filter, SPAD single photon counting avalanche photodiode. (b) Spontaneous Raman spectrum of a lipid droplet taken in a living cell. Highlighted is the peak location of the aliphatic C-H stretch vibration used for CARS imaging (2845 $cm^{-1}$). (c) CARS micrograph of a lipid-treated rat hepatocyte. (d) CARS micrograph of a lipid-treated human monocyte.

**Figure 11:** (a) Schematics of our time-correlated single photon counting CARS microscope. Abbreviations: BS beam splitter, M mirror, OPO optically parametric oscillator, DL delay line, DM dichroic mirror, PP pulse picker, OL objective lens, CL condenser lens, SP short pass filter, TCSPC time-correlated single photon counting, CCD charge-coupled device, APD avalanche photodiode, PC personal computer. (b) Arrival time histogram of epi-CARS (E-CARS) photons and back-reflected forward CARS (F-CARS) photons arriving at the photodetector. Note that the F-CARS peak is delayed by an extra ~ 2 ns due to the extra distance that the photons have to travel between the sample and the mirror that is used to reflect the forward-scattered CARS photons. (c) Overlay of E-CARS (green) and F-CARS (red) images of adiopytes in culture. (d) Line section through the adipocytes.

**Figure 12:** Principles of time-correlated single photon counting (TCSPC). (a) Electronics. (b) Timing of TCSPC signals, (c) Arrival time histogram of a signal consisting of multi-photon excited fluorescence and CARS contributions.

**Figure 13:** CARS and multi-photon excited CARS images of a section of a rat artery. (a) Combined signal with arrival times shown in false color. (b) CARS signal extracted by applying a short time gate. (c) Fluorescence signal extracted by applying a long time gate.

**Figure 14:** (a) Transmission electron micrograph (TEM) of a solid gold nanoparticle. (b) TEM image of a hollow gold nanosphere with 5 nm shell thickness. (c) Absorbance spectrum of a solution of 30 nm diameter hollow gold nanospheres.

**Figure 15:** (a) Raman spectra of a pH active SERS nanoprobe at low (pH 5) and high (pH 12.3) pH. The insets depict the change in the 4-mercaptobenzoic acid molecules bound to the nanoparticle surface. (b) SERS spectra of a single pH sensitive nanoparticle obtained under continuous illumination over 20 min. The reason for the varying Raman signal strength are fluctuations of the laser intensity of the 632.8 nm laser used to obtain the spectra.

**Figure 16:** (a)-(d) Snapshots of a sequence of darkfield micrographs of gold nanoparticles diffusing inside a bovine endothelial cell. Uptake to the cell was induced by functionalizing the nanoparticle surface with the TAT-peptide sequence of the HIV transduction domain. The restricted diffusion of the nanoparticles indicates uptake by endocytosis.

## Figures

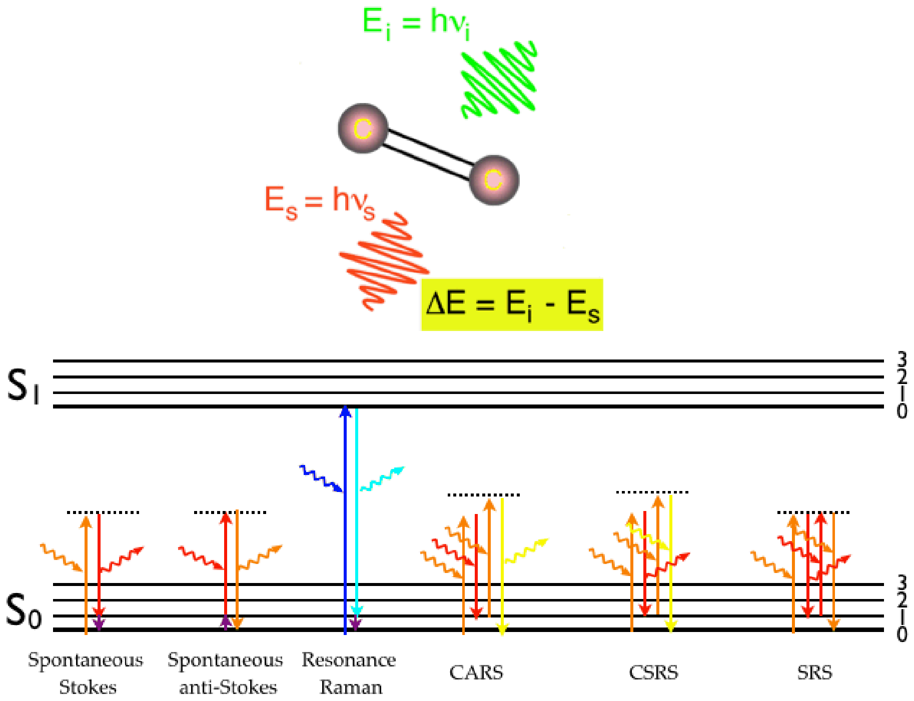
$E_i = h\nu_i$
$E_s = h\nu_s$
$\Delta E = E_i - E_s$
$S_1$
$S_0$
3
2
1
0
3
2
1
0
Spontaneous Stokes
Spontaneous anti-Stokes
Resonance Raman
CARS
CSRS
SRS

Chan et al., Figure 1

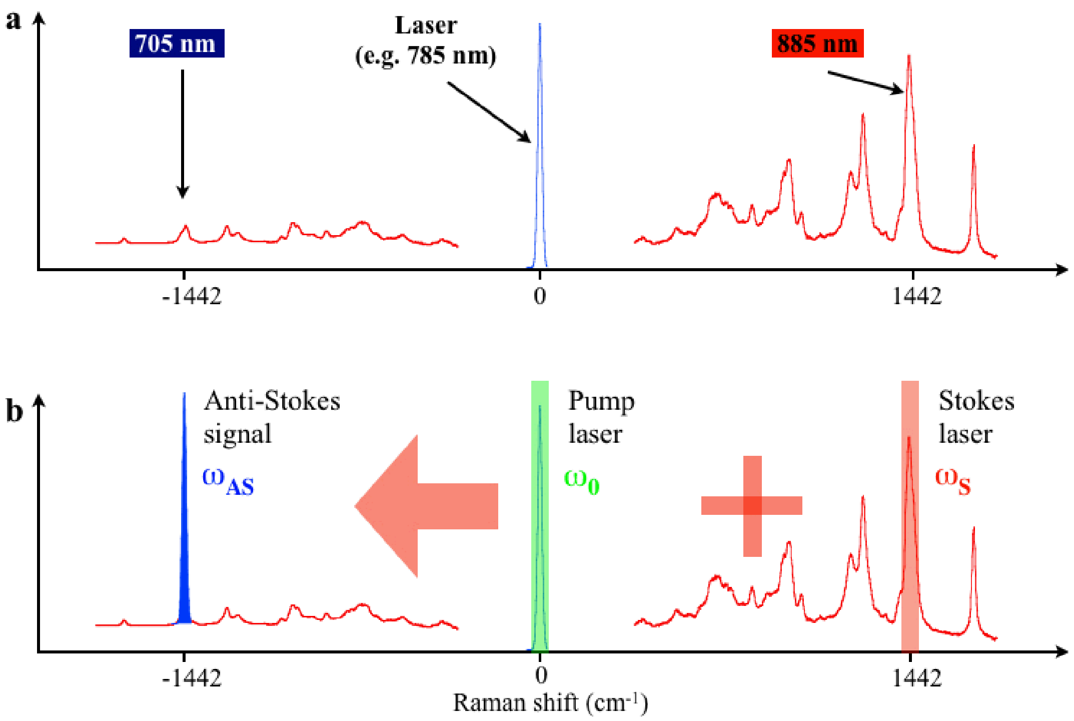

Chan et al., Figure 2

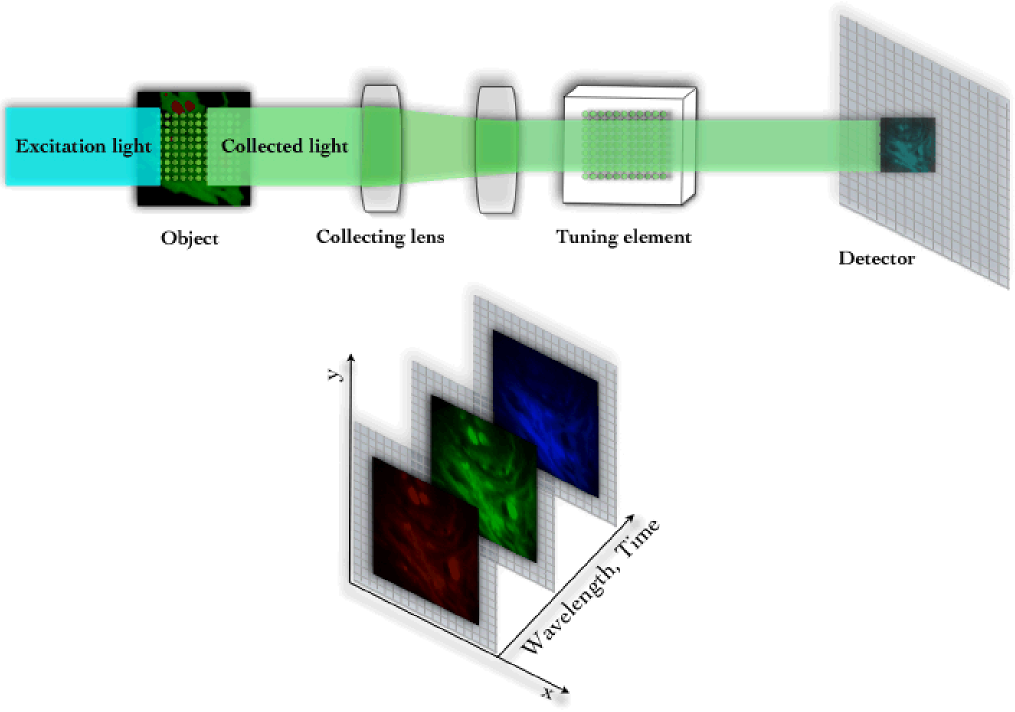
Excitation light
Collected light
Object
Collecting lens
Tuning element
Detector
y
Wavelength, Time
x

Chan et al., Figure 3

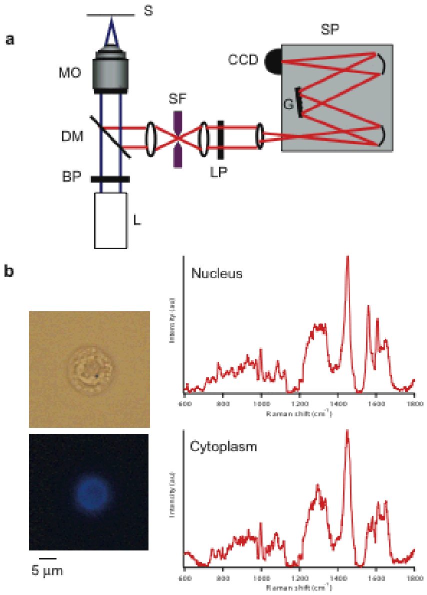
a
S
SP
CCD
MO
SF
G
DM
LP
BP
L
b
Nucleus
Intensity (au)
600
800
1000
1200
1400
1600
1800
Raman shift (cm$^{-1}$)
Cytoplasm
Intensity (au)
600
800
1000
1200
1400
1600
1800
Raman shift (cm$^{-1}$)
5 µm

Chan et al., Figure 4

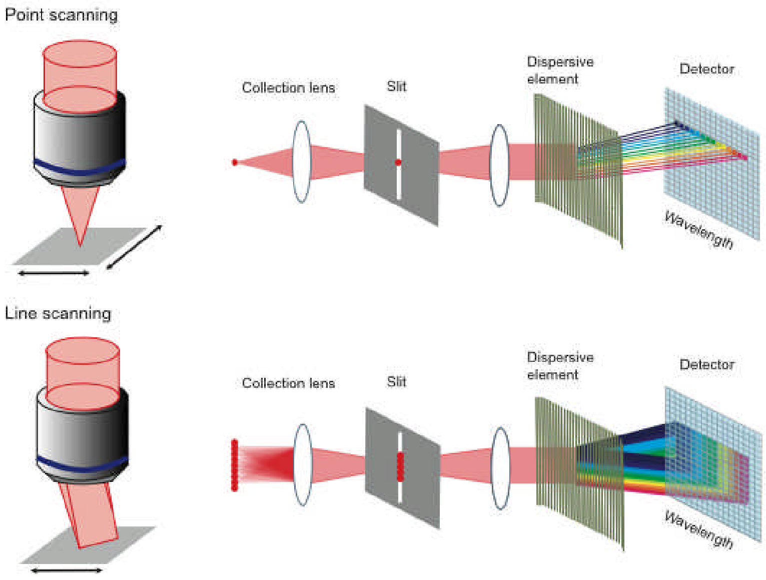
Point scanning
Collection lens
Slit
Dispersive element
Detector
Wavelength
Line scanning
Collection lens
Slit
Dispersive element
Detector
Wavelength

Chan et al., Figure 5

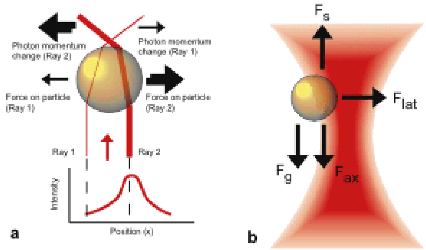
Photon momentum change (Ray 2)
Photon momentum change (Ray 1)
Force on particle (Ray 1)
Force on particle (Ray 2)
Ray 1
Ray 2
Intensity
Position (x)
a
$F_s$
$F_{lat}$
$F_g$
$F_{ax}$
b

Chan et al., Figure 6

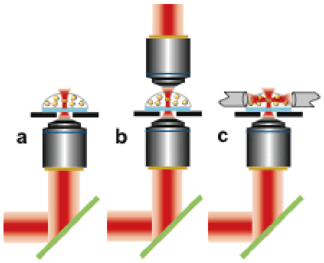

Chan et al., Figure 7

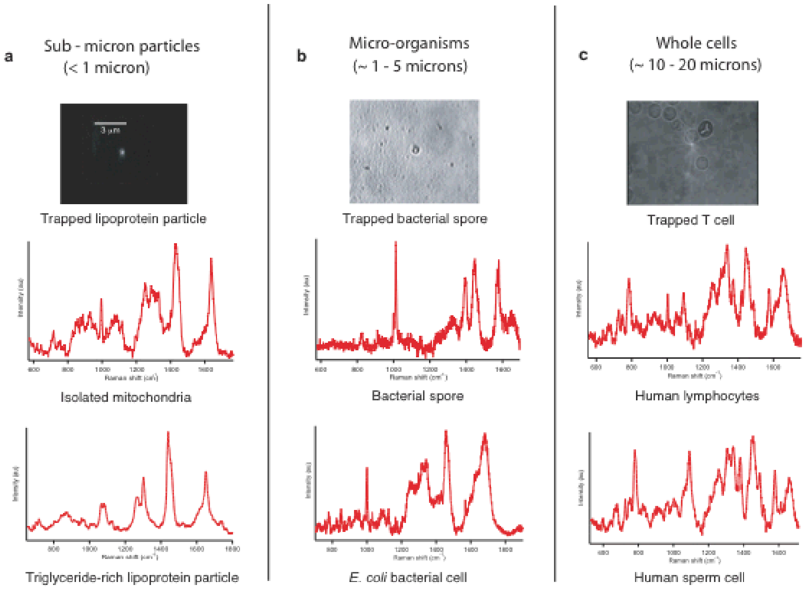

Chan et al., Figure 8

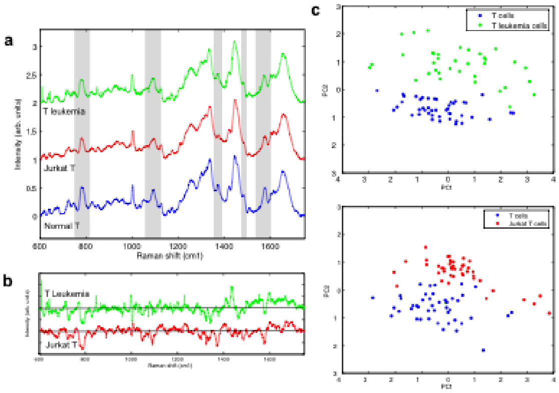

Chan et al., Figure 9

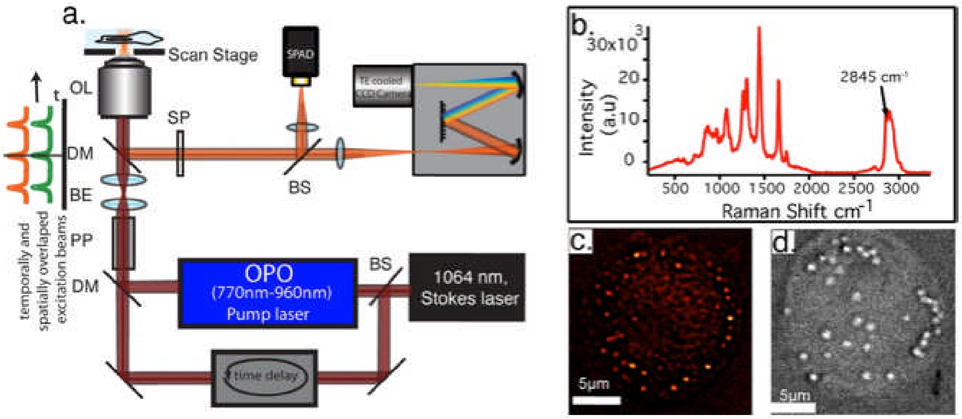
a.
Scan Stage
SPAD
TE cooled CCD Camera
OL
t
SP
DM
BE
PP
DM
BS
BS
temporally and spatially overlaped excitation beams
OPO (770nm-960nm) Pump laser
1064 nm, Stokes laser
time delay
b.
30x10^3
20
10
0
Intensity (a.u)
2845 cm-1
500 1000 1500 2000 2500 3000
Raman Shift cm-1
c.
5μm
d.
5μm

Chan et al., Figure 10

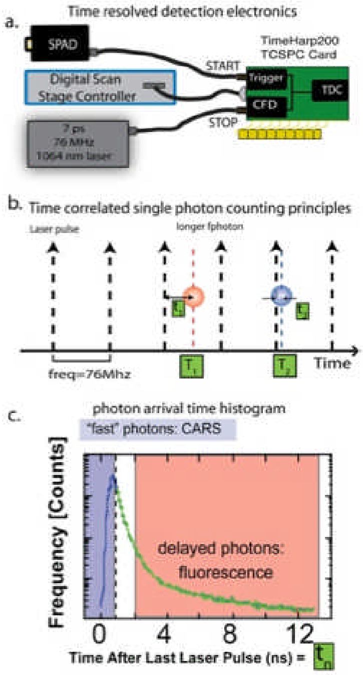
a.
Time resolved detection electronics
SPAD
Digital Scan
Stage Controller
7 ps
76 MHz
1064 nm laser
START
STOP
TimeHarp200
TCSPC Card
Trigger
CFD
TDC
b. Time correlated single photon counting principles
Laser pulse
longer fphoton
$t_1$
$t_2$
$T_1$
$T_2$
Time
freq=76Mhz
c.
photon arrival time histogram
"fast" photons: CARS
delayed photons:
fluorescence
Frequency [Counts]
0
4
8
12
Time After Last Laser Pulse (ns) = $t_n$

Chan et al., Figure 11

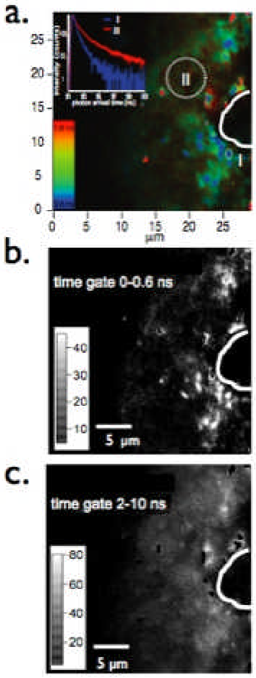
a.
I
II
25
20
15
10
5
0
0
5
10
15
20
25
µm
b.
time gate 0-0.6 ns
40
30
20
10
5 µm
c.
time gate 2-10 ns
80
60
40
20
5 µm

Chan et al., Figure 12

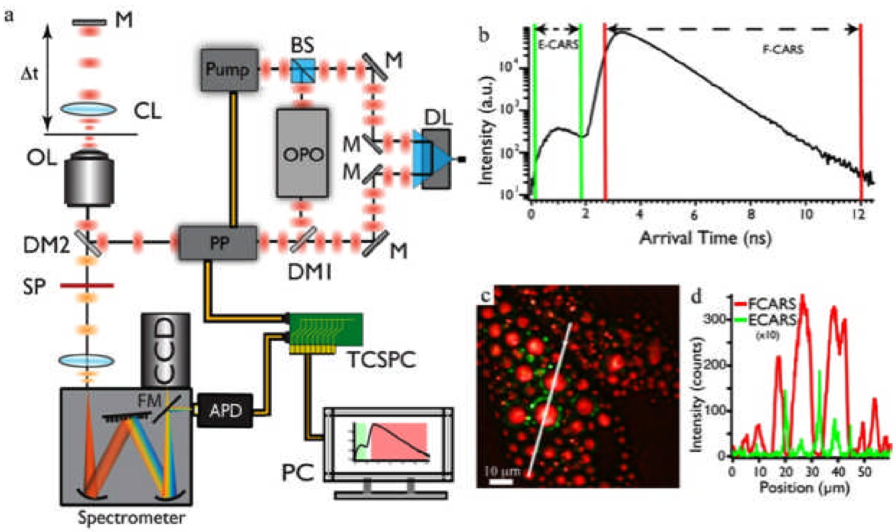
a
M
Δt
CL
OL
DM2
SP
CCD
FM
APD
Spectrometer
Pump
BS
M
OPO
M
M
DL
PP
DM1
M
TCSPC
PC
b
E-CARS
F-CARS
Intensity (a.u.)
$10^1$
$10^2$
$10^3$
$10^4$
0
2
4
6
8
10
12
Arrival Time (ns)
c
10 μm
d
FCARS
ECARS
(x10)
Intensity (counts)
0
100
200
300
0
10
20
30
40
50
Position (μm)

Chan et al., Figure 13

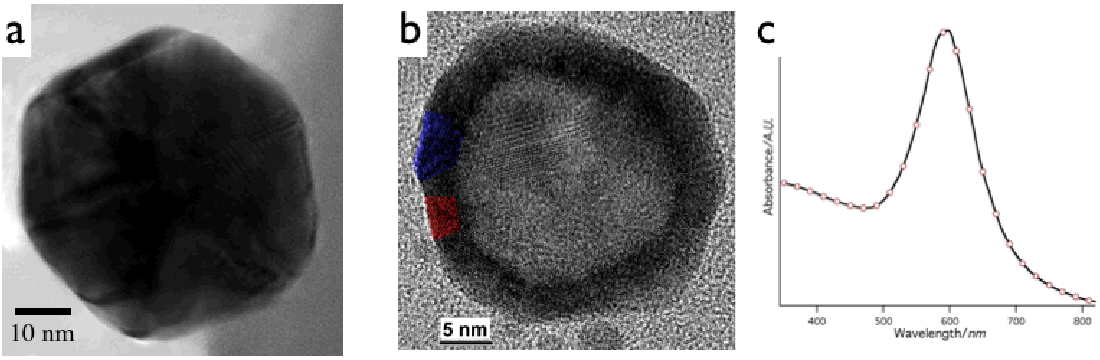
a
10 nm
b
5 nm
c
Absorbance/A.U.
400
500
600
700
800
Wavelength/nm

Chan et al., Figure 14

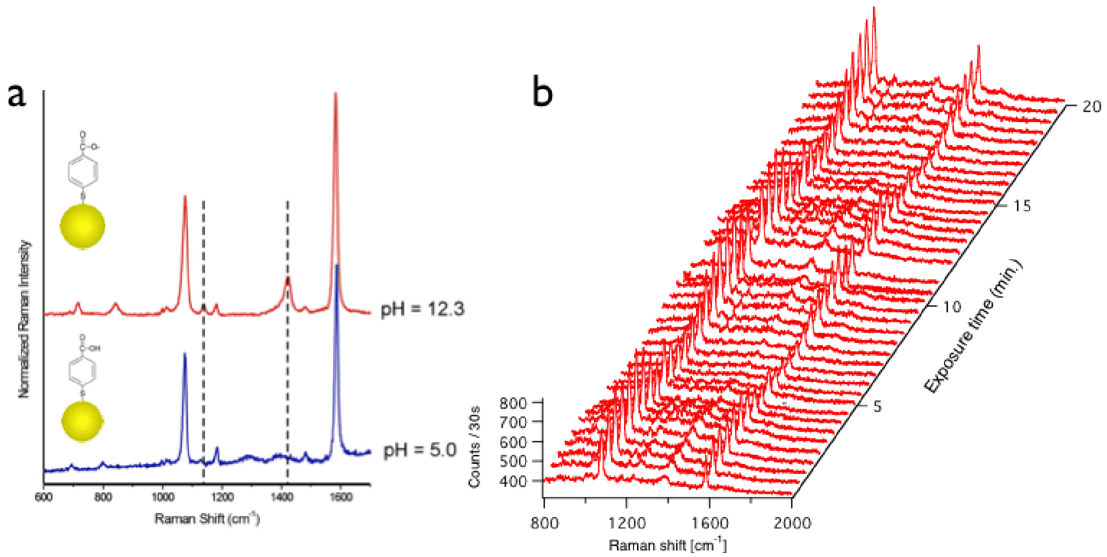

Chan et al., Figure 15

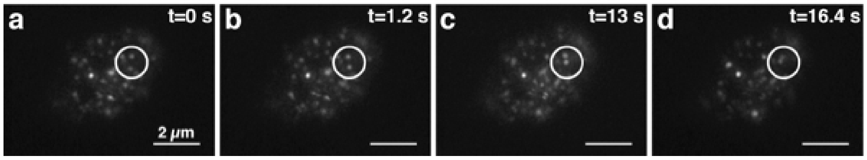
a
t=0 s
2 μm
b
t=1.2 s
c
t=13 s
d
t=16.4 s

Chan et al., Figure 16